EXPERIMENTS ON TRANSITIONAL REGIME SEDIMENT DENSITY FLOWS AND RESULTING DEPOSITS

BY

ZACHARY D BARNAAL

THESIS

Submitted in partial fulfillment of the requirements
for the degree of Master of Science in Civil Engineering
in the Graduate College of the
University of Illinois at Urbana-Champaign, 2016

Urbana, Illinois

Adviser:

Professor Gary Parker

Abstract

Much remains unknown regarding the sedimentary deposits of submarine density flows. Certain density flows may transition from a more turbulent to a more coherent flow regime e.g. by a loss of velocity in flows with large concentrations of suspended sediment. Such transitional flows are produced when turbulence becomes suppressed due to entrainment of cohesive sediment or from flow deceleration. Argillaceous sandstones and linked turbidite-debrites are types of submarine sediment deposits in a category known as hybrid event beds, and are interpreted to be emplaced by transitional regime flows (Talling, 2007; Davis, 2009; Haughton, 2009; Hodgson, 2009; Baas, 2011; Lee, 2013; and Talling, 2013). Sediment density current experiments have been conducted in a submerged flume to physically model such transitional flows. Correlations between the properties of the flows and the properties of the deposit exist and the results allow us to better understand sediment density currents with deterministic rheology and the resulting geology.

To my family

Contents

1 Introduction

Sediment density flows transport some of the largest volumes of sediment among all mechanisms on Earth. The flow and sedimentary processes are of interest because much is left unknown about their properties. A variety of different types of sediment density flows have been previously defined based on experiments, flow observations, and interpretations of deposit geology. Such deposits include sediment beds of a particular type called hybrid event beds (HEBs) that are the focus of this project. Flume experiments conducted on these types of flows allow us to understand the rheology that determines HEB geology. The experiments are physical models of events that may not be easily studied directly in the field; such experiments, even though they may not represent precise models in the sense of similitude, give insight into the origin and formation of real-world sedimentary structures.

Properties of transitional-regime density flows, resulting depositional processes, and corresponding sedimentary structures are the focus in the experiments conducted for the present project. The experimental setting and methods involved in previous experimental work on sediment gravity flows were considered and applied to this project (Postma, 1988; Garcia, 1989; Garcia, 1993; Mohrig, 1998; Marr, 2001; Harbitz, 2003; Toniolo, 2003; Ilstad, 2004; Lamb, 2004; Toniolo, 2006; Yu, 2006; Sumner, 2008; Baas, 2009; Sequeiros, 2009; Spinewine, 2009; Sumner, 2009; Sequeiros, 2010; Baas, 2011; Cantelli 2011; Manica, 2012; Cartigny, 2014; Patacci 2015). The results on flow and deposition obtained for the experiments were analyzed under previously-proposed theoretical flow and deposition frameworks. Previous sedimentary field observations are considered to compare experimental results and discuss interpretations. Our ultimate findings will be used to develop additional capabilities in numerical models of dilute, transitional and concentrated density currents and resulting deposits.

1.1 Field Observations and Interpretations

Dilute turbidity currents laden with sand suspension have been found to emplace limited sheet-like deposits and submarine fans (Xu, 2004). Dilute turbidity currents driven mostly by mud may often construct leveed channels on submarine fans. The levees of these channels may consist of mud, but the flows may also carry a significant amount of sand that composes the channel deposits. The fans emplaced by dilute currents with mud can extend out hundreds to thousands of kilometers (Pirmez and Imran 2003). Deposits emplaced by dilute flows with more turbulent rheology include turbidites that may be mostly sands, but with finer particles like silts or clays and coarser particles like gravel (Postma, 1988; Yu, 2006; Stevensen, 2014)

Sediment gravity flows with larger concentrations or within a less turbulent flow regime may deposit more massive turbidites and/or deposits with relatively coarser grains (Agirrezabala, 1994; Kneller, 2000; Yu, 2006; Kostic, 2007; Sequeiros, 2009; Spinewine, 2009; Cantero, 2011). It has been previously determined that relatively coarser deposits tend to be emplaced within channels, on relatively steep slopes, and/or proximal to the sediment source. In many cases, however, coarse grains and clasts may be carried out to less proximal locations; e.g. the beds found in the Basque-Cantabrian region, west of the Pyrenees (Agirrezabala et al. 1995). More commonly it has been interpreted that such grains are carried out by "powerful" turbidity currents, meaning higher velocity flows in the more turbulent flow regime.

Debris flows are sediment density currents with even greater sediment concentrations. Debris flows have lower turbulence and often contain very fine sediment that may supports grains orders of magnitude larger. Debris flow deposits are known as debrites and contain signatures of the flow description such as conglomerates or deposits with gravel supported in a matrix of clay or silt. There may be many different origins for debris flow i.e. submarine slope failure resulting in a slump. (Winn and Dott, 1977; Lowe, 2000; Sohn. 2000; DeBlasio, 2004; Toniolo, 2004; Lastras, 2005). Of particular interest, coarse grains and mud clasts may also frequently be found among the sand-mud matrix

within HEB deposits. (Haughton, 2009; Hodgson, 2009; Davis, 2009; Baas, 2011; Kane, 2012; Talling, 2013; Patacci, 2014; Fonnesu, 2015; Southern, 2015)

HEBs are sediment beds with deposits containing sediment characteristic of both more cohesive flows and less cohesive flows. An example of a more cohesive flow is a high-concentration debris flow, where dispersive pressure supports dense volumes of finer material (clays) that are a signature in a portion of HEB deposits. The less cohesive flows where turbulence entrains and supports coarser material (sands) leave a different signature in another portion of the bed. Debris flows may transition downstream to turbidity currents with turbulence enhancement such decreasing flow concentration. Alternatively, turbidity currents may transition to cohesive flow with turbulence suppression, perhaps associated with a loss in flow velocity. In HEBs there is no clear separating bed boundary between the two deposits, suggesting that the complex structure of HEBs derive from the same event. (Hampton, 1972; Haughton et al. 2009).

The present report considers a specific type of HEB deposits called argillaceous sandstones which have been found to be deposited by the previously defined transitional-regime sediment gravity flows. Argillaceous deposits refer to sandstones or sandy deposits that contain a range of clay content in the matrix. The clay content in argillaceous deposits is significant in reducing the amount of pore space and cause a large reduction in the hydraulic conductivity of the argillaceous sandstones. Although beds with such properties could be deposited as a result of multiple transport events, it is interpreted that HEBs are emplaced by single events from flows with rheology in the transitional regime (Talling, 2007; Davis, 2009; Haughton, 2009; Hodgson, 2009; Baas, 2011; Lee, 2013; and Talling, 2013).

There are known real-world sedimentary structures such as HEBs with origins and features that are not sufficiently understood. There are multiple examples of Ground Penetrating Radar (GPR), core samples, and field observations that include HEB deposits such as argillaceous sandstones. Field examples include HEBs of the Outer Forties Fan, UK and Karoo Basin, South Africa. GPR and coring has also identified examples of

HEBs among: the Ulleung basin, Sea of Japan; the Agadir basin, Madeira, Morocco; and of particular interest the Mississippi main fan including the Wilcox Formation, Gulf of Mexico (Talling, 2007; Davis, 2009; Haughton, 2009; Hodgson, 2009; Lee, 2013; Terlaky, 2013; Stevenson, 2014; Fonessu, 2015).

The Wilcox Formation in the Gulf of Mexico includes bed types that range from debrites to turbidites including HEBs. The stratigraphy determined from core samples and GPR is commonly a general sequence of turbidites overlain by argillaceous and/or linked deposits, and then debrites. The vertical patterns are interpreted to represent horizontal bed configurations, but these are superimposed due to lobe progradation over antecedent deposits. It is speculated that a transition from channelized flow to less confined lobe-like flows drives the transformation from more laminar to more turbulent conditions, which leads to the emplacement of a progression of linked turbidite-debrite deposits (Kane and Pontèn, 2012). It is common found that HEBs are in the distal reaches of deep-sea density current systems. It has been proposed that HEB deposits may also be emplaced in proximity to the sediment flow source. In the present project we are attempting to study a range of cases of flows leading to HEBs.

1.2 Previous Density Flow Experiments

There has been much research involving physical models and experiments on sediment density flows that emplace deep-sea deposits. More recent work includes experiments to explore the rheology of a variety of flow types. Previous categorization of sediment gravity flows has identified turbidity currents with low-density flows and submarine debris flows with high-density flows. The rheology, depositional patterns, and corresponding sedimentary structures of the two distinct types has been previously defined (Mohrig et al., 1998; Marr et al. 2001; Yu et al. 2006, Talling et al. 2013). There is work that also includes examples of deposits that are not considered to be emplaced by one type of flow or the other, but may instead represent the deposit from a transitional flow regime. The geology of these deposits has been previously explained by certain extensions of the

concepts of either turbidity currents or debris flows.

Previous density current experiments on either turbidity currents or on submarine debris flows tend to converge toward a common description. Turbidity currents are predominantly lower-concentration flows carrying and depositing an abundance of sand-size sediment that are supported mostly by turbulence. Turbidity currents with higher-concentration or stronger cohesion may emplace coarse-grained (e.g. sand with gravel) deposits that are more common in debris flows. Debris flows are flows with much higher concentrations and are composed of, and tend to deposit, silts and clays. Debris flows may carry much coarser material with support by dispersive pressures, particle interaction and buoyancy of the matrix.

Alternatively, turbidity currents that are composed completely of dilute suspended clay and silt will tend to deposit those fines, but at slower rates. There may also be debris flows with large volumes of mud that deposit no sand or gravel. These often travel a relatively shorter distance from a source than turbidity current run-out. In other findings, however, the mud rheology or the effect of hydroplaning can often cause such currents to run out to as much as 100 km (Mohrig et al., 1998; De Blasio et al. 2004; Elverhøi, 2005; Issler, 2005). Debris flows containing significant amounts of sand and sufficient mud matrix to prevent the loss of pore pressure may also allow the flow to propagate downslope, resulting in similar depositional lengths (Marr et al., 2001; Toniolo et al. 2004).

There are nevertheless sediment density flows and deposits that may not be easily defined in terms of previously-described rheology. These flows are within a transitional regime between debris flows and turbidity currents. Among these are flows that have been categorized as turbulent, transitional, and quasi-laminar phases based on estimates of the Reynolds number of the flow (Baas, 2009). Transitional regime flows produce a variety of deposits with structures and patterns that are not completely defined. Recent work with experiments and physical models, and in particular those observed in the present project, help characterize the origin, mechanics and fate of such transitional flows, as well

as flows that deposit HEBs including linked-debrites or argillaceous sandstone (Sumner et al. 2009; Baas et al., 2011).

Previous experiments on turbidity currents and debris flows that are either fully turbulent or fully laminar have not explicitly been reported to emplace deposits with properties similar to those of HEBs. Instead, transitional-regime sediment flows have been found in previous experiments to result in deposits that correspond to certain HEBs (Sumner, 2008; Baas, 2009; Sumner 2009; Baas 2011). These sedimentary structures found in core samples and field examples have become of particular interest because the nature of HEBs are not well-understood, and their structure has implications on the recovery of deep water hydrocarbons. Much still remains to be discovered regarding transitional flows and sedimentary deposits related to HEBs. This motivated a survey of literature on the transformation of flow rheology and analysis of the beds and their evolution, which was conducted prior to the experimental program reported below.

1.3 Numerical and Theoretical Considerations

Experimental parameters are set, measured, or recorded to quantify the properties of the rheology and geology at various streamwise locations for each run. In reference to previous experimental work, the dimensionless Reynolds number Re of the flows are computed. R_e is a ratio of inertial force and viscous force, and allows us to better understand turbulence properties of the flows. R_e is defined in Eq. 1 where U is the layer-averaged velocity, h is the flow thickness, and ρ_m is the flux-averaged density of the sediment flow. ρ_m is determined by Eq. 2 where the parameter C is the flux-averaged volumetric concentration of sediment in the current, u is the velocity at x distance from the bed, c is the sediment concentration at x distance from the bed, and μ_m is the dynamic viscosity of the fluid. μ_m is increased above the standard range of values for pure water by e.g. the presence of suspended kaolin clay. μ_m may be approximated in Eq. 3 as the formulation for kaolin mixture flows from Baas (2009) and C may be found with Eq. 4 .

Another important parameter to consider is the flow Richardson number R_i as in

Eq. 5. R_i is a dimensionless ratio of buoyant force to inertial force of the current. R_i is also commonly expressed as the densimetric Froude number F_{rd} as defined in Eq. 6 corresponding to the square-root of the inverse of R_i, where R is the submerged specific gravity of the sediment in the current mixture, g is the acceleration of gravity assumed to be constant at $9.81 m/s^2$, and θ is the slope angle of the bed. The results are dimensionless parameters where R_i helps to determine the scale of mixing and R_e helps to determine the state of turbulence of the sediment density flows.

One main factor considered for the characterization of the sediment beds is the relative content of fines, i.e. material in the silt-clay range. Deposits with significant content of fine grains are particularly relevant for the type of HEB with argillaceous deposits. In the experiments that we have conducted in a scaled setting, the sediment size that may correspond to mud sizes in the flume deposits is different from those in natural, field scale deposits. A particle fall velocity scale was conducted for scaling including the grain sizes D to determine argillaceous content. Fall velocity v_s is calculated in m/s from Eq. 7 where R_f is the dimensionless fall velocity using the formulation of Eq. 8 from Dietrich in 1982; the coefficients $b_1 ... b_5$ are defined in Table 1, and R_{ep} is the particle Reynolds number defined in Eq. 9 with υ as the kinematic viscosity of water.

Table 1: Coefficients of $b_1 ... b_5$ for Eq. 8.

b_1	2.891394
b_2	0.95296
b_3	0.056835
b_4	0.002892
b_5	0.000245

The word 'argillaceous' refers to rocks or sediment containing clay mineral clay-size grains. The grain size that we may consider in the field-scale to be argillaceous may be in excess of the definition of 2 microns which was used to define the clay size range, and indeed may range up to 10 microns in the case of kaolinite. According to the fall velocity scaling that is used in analysis of the experiments, sediment with an equivalent spherical diameter 11.2 microns is taken to be argillaceous. Therefore any grain size D_a $\leq$ 11.2 μ m, or smaller is used in the quantification of the fraction content in a sample

that is argillaceous. The argillaceous fraction content A_c is computed as follows. The sediment is divided into M size ranges, each with characteristic size D_i and mass content fraction f_i, $i = 1..M$, defined as in Eq. 10. One of these ranges, i.e. the range $i = m$ is chosen such that its upper bound has size D_a. The fraction content that is argillaceous A_c is then given as in Eq. 11.

$$R_e = \frac{Uh\rho_m}{\mu_m} \tag{1}$$

$$\rho_m = \rho_s C + \rho_w(1 - C) \tag{2}$$

$$\mu_m = 0.0001 + 0.206C^{1.68} \tag{3}$$

$$C = \frac{\int_0^h uc \, \mathrm{d}x}{U} \tag{4}$$

$$R_i = \frac{RgCh}{U^2} \tag{5}$$

$$F_{rd} = {R_i}^{-1/2} \tag{6}$$

$$v_s = R_f \sqrt{RgD} \tag{7}$$

$$R_f = e^{-b_1 + b_2 ln(R_{ep}) - b_3 [ln(R_{ep})] - b_4 [ln(R_{ep})]^3 + b_5 [ln(R_{ep})]^4} \tag{8}$$

$$R_{ep} = \frac{D\sqrt{gRD}}{\upsilon} \tag{9}$$

$$\sum_{i=1}^{M} f_i = 1 \tag{10}$$

$$A_c = \sum_{i=1}^{m} f_i \tag{11}$$

2 Experimental Methods

A series of exploratory and main-set experiments were conducted in order to reproduce argillaceous sand HEBs in a scaled physical model. The flows in the experiments were run in a flume and sloping ramp with capability to convey and measure sediment-driven underflows. A total of 43 runs were conducted. Among these we apply 154 sets of measurements from the main experiments which all include measurements of flow velocity, flow concentration, depositional record and bed evolution. The measurements are used to determine if the results are consistent with HEBs of interest that have been described in the field. A detailed flow analysis and depositional record was completed during each run. The results are applied to interpret the origin, fate and scale of real-world scale HEB settings.

2.1 Experimental Setup

The experiments were conducted in the density current tank of Ven Te Chow Hydrosystems Laboratory (VTCHL) at the University of Illinois. The density current tank is first filled with freshwater as shown in Figure 1. The study area of the tank is $15m$ in length, $0.45m$ in width, $1.4m$ in depth, and contains a flume platform with sloping ramps with the capability to convey and measure a variety of density flows. Slurries of water and sediment are pumped into the flume with the use of a diaphragm pump from a nearby mixing vessel with $4.5m^3$ capacity as in Figure 2. The inlet on the upstream end of the tank consists of a $0.0381m$ diameter hose leading to a T-shaped diffuser as in the diagram in Figure 3 from Sequeiros (2009). The diffuser allows the slurries to flow uniformly across the width of the flume. The input flow rate was measured by a magnetic flow meter; discharges to $20L/s$ of the slurries could be measured with $\pm$ $0.005L/s$ precision.

Sections along the length of the tank were labeled according to a specific convention for organization. The six sections are labeled respectively from upstream to downstream as alpha, beta, gamma, delta, epsilon, and zeta (Roman rendition of the

first six letters of the Greek alphabet) as in Figure 1. The flume bed was built for the first set of experiments to allow for sloping surface and slope-breaks as shown in 3D drawing of Figure 4 and the photograph of Figure 5. The bed was composed of three panels each 2.44 m in length that span the width of the tank. The panels were suspended by stainless steel wire to be held in place yet be easily adjusted to variable heights. The slopes were adjusted from 3° - 10° for the upstream panel in section alpha, the center panel in section beta from 0° - 3°, and again 3° - 10° for the downstream panel in section gamma (Figure 4). The configuration there again breaks slope to the horizontal bottom of the tank spanning the remainder of the length of the tank in sections delta, epsilon, and zeta (Figure 1). The slope breaks were designed to create conditions for changing flow regimes that might be conducive to create sediment flows in the transitional regime and the emplacement of HEBs.

The initial bed slope of 5° shown in Figure 5 was low enough that the sediment in the flow deposited out passively. After the first few experiments, however, proximal deposition caused the bed slope to steepen to the point at which the flow could carry sediment significantly farther downstream. The flow continued to steepen in subsequent runs to the point that it became unacceptably high from the point of view of measurement. Sediment mixing into the ambient water causes murkiness, and thus problems for visibility and instrument use. Although flow deposits can be stacked one atop the other, at some point it is necessary to drain the tank and excavate the deposit after all flow, deposit, and bed geometry measurements are conducted. After one set of experiments and tank draining the seal between the tank and the flume failed, and repairs were necessary.

It was determined by trial and error that a series of slope breaks were not necessary to create acceleration and deceleration conditions consistent with transitional regime flows. Suspending the flume panels was also problematic. Therefore a new design was installed which consists of a single $4.87m$ length sloping region followed by a break to a $7.62m$ length horizontal region, as shown in Figure 6. A wider damping tank farther downstream, which is visible in Figure 1, allows the dense slurries to be bottom-drained while adding makeup freshwater at the surface. This procedure suppresses the pollution

of ambient tank water by sediment-laden water from the underflow. The setup was sufficient for running multiple experiments and is the final setup ultimately used in all of the runs providing data for the project.

The sediments used in the experiments are various mixtures of a commercially available kaolin clay called Edgar Plastic Kaolin (EPK) and a commercially available silica flour called Sil-Co-Sil 250. The kaolin serves as a surrogate for cohesive muds, and the silica serves as a surrogate for non-cohesive fine-sand or gravel. The material properties of the kaolin are shown in Figure 7 and the grain-size distribution (GSD) of the kaolin is given in Figure 8. The material properties of the silica are shown in Figure 9 and the GSD is given in Figure 10. The GSDs of both materials were determined using a commercial particle sizer (Malvern Mastersizer 3000E). The Mastersizer allows for ultrasonic dispersion for breaking up flocs and aggregates to their constituent particles; more details about the Mastersizer is described in greater detail below. Ultrasonic dispersion was not used in determining the GSDs of Figure 8 and Figure 10.

The variable input parameters used to adjust flow conditions throughout the experiments were the volumes of kaolin, silica, and fresh water combined into the mixing tank. The variable mixtures create the slurries that were run in the experiments which result in a wide range of the different categories of sediment density flows. Table 2 summarizes the input parameters for the variable mixtures in all of the experiments conducted. The experimental sets include 1%, 3%, 5%, 10% and 20% total concentration all run for mixtures with volume percentages of 30% silica and 70% kaolin, 40% silica and 60% kaolin, 50% silica and 50% kaolin, then 70% silica and 30% kaolin. It is important to note that the 1% and 20% total concentration runs were not done for all combinations of the mixtures because of redundancy. Other input parameter variables could be important, yet the range of the sediment density flows have flow results that span across the transitional regime by solely adjusting the input sediment concentration.

Table 2: Table of the main set of experiments. Runs with various total sediment concentrations (vertical) and their different sediment types (horizontal) may be found with the identity of the experiments conducted (Run IDs).

Percentages	1%	2%	5%	10%	20%
Pure kaolin	-	Bound 5	Pulse 3	Pulse 4	Bound 1
30 sil 70 kao	Main 10	Main 1	Pulse 1	Main 12	Bound 4
40 sil 60 kao	Show 1	Show 2	Main 9	Main 8	-
50 sil 50 kao	Main 4	Main 3	Main 2	Explore 2	Explore 1
70 sil 30 kao	-	Main 7	Main 6	Main 5	-
Pure silica	Pulse 2	Main 11	Bound 3	Bound 2	-

2.2 Flow and Sediment Transport Measurements

Flow velocities within the sediment density currents were obtained with the use of an Ultrasonic Velocity Profiler (UVP). The UVP transmits packets of ultrasonic frequencies from a transceiver directed at some set angle along downward-normal profiles. The packets ping into a flow and some of the signal reflects back into the transceiver. The transceiver also is a transducer which applies the Doppler shift principle where the sent and received packets become resolved for flow velocity at discrete points along the profiles. The information then compensates for the angle of approach to result as instantaneous velocity measurements relative to a fixed bed at the points along the vertical profile. Some examples of the resulting velocity profiles collected are displayed in Figure 11 - Figure 14. In the experiments, up to two transducers are used simultaneously and are easily moved to a variety of locations throughout the time of each run.

Sample volumes of the flow were collected in-situ from within the density currents at various times and locations during the flow runs. The samples were extracted with the use of rods placed in the flume that had siphon tubes attached at fixed distances along the vertical. The samples were then measured for sediment concentration to obtain sediment concentration profiles of the flow in a method described below. Immediately following each completed run, deposit samples on the bed were also collected from locations along the length of the flume. A scoop with a long handle and spring-loaded gate was used to carefully extract only the most recent deposit. The bed samples were extracted to conduct sediment analyses in order to determine grain type and to obtain GSDs. The

techniques used in the sediment analysis is also described in more detail below.

The technique to determine concentration profiles at each location, in-situ sample volumes were extracted from elevations within the flow corresponding with the vertical profiles where velocity measurements were taken. Siphon rakes, composed of rods mounted with slides and fixed siphon tubes, were built to sample at different locations and at appropriate times during each run. Each siphon rake consists of four tubes set $10cm$ apart, with the bottom-most siphon commonly set at $1cm$ from the bed. All siphoned samples were collected separately in small containers for the concentration and grain-size analyses discussed in the methods section below. Example profiles of the upward-normal sediment concentration variation within a density flow are displayed in Figure 15 and Figure 16. Figure 16 corresponds to section beta, upstream of the slope break, and Figure 15 corresponds to section epsilon, downstream of the slope break (Figure 1).

The bed deposit samples were collected immediately after each run to sample the deposits without getting the cap of very fine-grain material that settles out from sediment that slowly comes out of suspension in the ambient water. The bed samples were extracted with the use of a manually operated scoop that reaches to the bed with a long arm and collects the material. A mechanical lever is pulled so as to cap the scoop, ensuring that the collected sample can be brought to the water surface and bottled without being lost in the ambient water. Suction through siphons was additionally used to collect bed samples. Bed samples at many locations along the bed were collected for sediment property and grain-size analysis with the methods described below in the sediment analysis section.

The evolution of the bed and the deposit geometry was recorded through photography. A set of cameras were positioned during each run to video-record the flow and bed evolution. Photographs of the deposits along streamwise sections of the flume were captured with a transparent grid for scale taped to one glass sidewall. The photos were applied to determine deposit thickness, bedform structures, layering patterns and composition features. The features such as kaolin content and settling caps may be identified from color and shading as discussed below. Videos and photographs as described

in Appednix C may be found in a supplemental file with the folder name "Video-Photo". Deposit features were additionally analyzed after each set of runs when the tank was drained. After draining, the bed again was excavated for samples. Full sediment analyses, as described in the sediment analysis section, were conducted as to compare to the in-situ samples taken immediately after the end of the run.

Some assumptions were made for the measurements of both the velocities and the samples of sediment-laden water obtained from the flow. These include the concept that the flow was fully developed by the time the measurements were conducted. This assumption is partly justified by the fact that we allowed some amount of time to pass after the initial head passed; thus the current was allowed to reach its quasi-steady state with time. Another assumption is that the flow at each point was not being influenced by its own backwater reflection from downstream. The reflection of the current may indeed influence some of the measurements, especially in the downstream locations. However, using layer averaged and flux averaged values, as is procedure described in the analysis section, may help mitigate any inaccuracy from the backwater reflections.

One important assumption is that the flow was indeed quasi-steady during the time all measurements were collected and all samples were extracted from the flow. The diaphragm pump used to feed the slurries into the tank creates a dampened pulsing action of the flow, however, it is assumed that the pulses are consistent and steady enough that the measurements collect the representative values of the flow over time. It is also important to note that there is some inherent error in the instruments used to collect measurements and data. More information on the uncertainty of measurements and results may be found in the following sections.

The instruments for either collecting or analyzing data have some known uncertainty to them. The UVP velocities are assumed to be the true velocities plus or minus the described precision of the instrument since there are no other methods accurate enough to compare the results to. Similarly, grain size analysis was performed with an instrument that is assumed give be the true values because any other method to compare does not

come close to the accuracy and precision of the instrument. The recorded geometry of the flow and the deposits are only as precise as the scale used to measure them, which is plus or minus $0.05cm$. The accuracy however is only as good as the ability of the individual recording. It is important to note that in all steps of the experiments, human error may be the main cause for inaccuracy or uncertainty.

In the experimental results perhaps the greatest source adding uncertainty is the human error in collecting bed samples for sediment grain-size and grain-type analyses. The scoop was relatively clunky to operate especially when sampling the thinner deposits. For some samples perhaps sediment deposited from previous runs were collected along with sediment of the antecedent run. For some other samples perhaps ambient water containing suspended sediment was collected along with the bed sample. In either case the analysis would perhaps include grains not representative of the bed deposit for that run. The grain-type and grain-size are very important measurements to have low error values of because their properties are directly used in the experiment results. The examples determined by such measurements are argillaceous content A_c as in Eq. 11 and kaolin content K_c as in Eq. 12 where V_k is volume of kaolin grains and V_c is volume of silica grains.

$$K_c = \frac{V_k}{V_k + V_c} \times 100\% \tag{12}$$

2.3 Analysis of Rheology

The UVP writes flow velocity data from each measurement into files for later access. The results of the UVP are of a specific format which include raw values of time, velocity, distance, and various other parameters. A code written in MATLAB by Pedocchi et. al in 2006 as in the Annex file under Appendix A organizes the UVP data and applies a function that determines the velocity for each time of each point along the vertical profile for that measurement. The function takes into account parameters set at the beginning of the measurement. The parameters include transmitted/received ultrasound properties,

ambient fluid properties, and angle of the measurement. The function organizes the resolved data which results in a matrix of velocities with distance (mm) from probe on one axis and time (ms) on the other axis.

A simple script then averages the velocities for each distance over any amount of time in the measurement. The result is automatically plotted as a representative velocity profile for that location and measurement period, as shown in Figure 17. Each velocity profile may then be averaged from the bed to the top of the flow thickness to resolve the layer averaged velocity U. It is important to note that velocities at points near the top of the flow thickness were often negative due to back-currents caused by the density flows themselves. The backflow causes and increase in the relative velocity when considering a Lagrangian field with the flow. This relative velocity that the flow feels has an effect on mixing and inertial actions which may need to be compensated for when considering the influence of velocity on parameters such as the Reynolds number.

2.4 Sediment Analysis

During the first runs an instrument by Sequoia called the Laser In-Situ Scattering and Transmissometer (LISST), in particular the LISST-Settling Tube (LISST-ST) product was used to determine the GSDs of the first samples collected. The instrument is a large torpedo shaped object containing an optical cell for sample volumes to pass through when sampling in open water. The particular model is modified to attach a settling tube onto the optical cell to conduct measurements in the laboratory as opposed to in the field. Laser light beams are sent through the optical cell containing a volume of the sample. The beams are diffracted off of grains at various angles depending on particle size. The scattered light is then detected by a series of 32 photovoltaic rings, and the various light intensity found in each ring is used by the LISST computer software to determine the relative quantity of grains in each size range.

The process for running through the LISST is as follows. The collected sample bottles were shaken up to be well-mixed. The measurement cell in the LISST requires

about $100mL$ of a solution that is not more concentrated than about 75 $\mu L/L$ or else it gives erroneous results. The concentration limit also depends on factors such as particle sizes, particle density, beam path length, and beam attenuation coefficient. To reach within the range of appropriate concentration, each sample was diluted with some known volume of deionized water. The diluted samples were then poured into the optical cell of the LISST to run one at a time. The LISST software, as shown in Figure 18, operates on a connected PC that determines and displays the sediment data such as GSDs.

The LISST uses the detected grains to find the concentration of grains in each size bin relative to the entire sample. The distribution of the concentrations in each bin then forms the GSD results that the program displays. The bin concentrations were all be summed together over the entire size range to get the concentration of the dilution that was input into the optical cell. The dilution concentration was then extrapolated across the added volume of deionized water in order to resolve for a representative concentration of each sample. However, the LISST does not give consistent values for total sediment concentration in comparison with a weighing method discussed later. Yet the LISST results have been applied in such manner in the past to obtain GSDs of sediment density currents (Pedocchi et al, 2006).

Weighing the samples was also used to determine sediment concentrations. The weight of foil measuring dishes were recorded then some amount of the each sample was poured into the dishes. The total weight of each sample plus dish was then recorded. The water of all samples was then evaporated off in a laboratory dehydrator leaving each dish with only the sediment that was in suspension. The samples with dishes were then weighed and recorded again. The weight of the dishes are subtracted both off of the initial total weight (with H_2O) and the final total weight (dehydrated). The water volume V_w then is equal to the total sample minus the baked sample per $1g/cm^3$. The sediment volume Vs then is equal to the dehydrated sample minus the dish weight per sediment density of $2.65g/cm^3$. The formula in Eq. 13 is then used to calculate the percent concentration by volume. One problem with this method is that there are three occasions when mass is measured in the process; thus more chance for human error on

top of the inherent errors in the measurement.

The laboratory acquired a new instrument for particle sizing after the first few experimental runs had been conducted. The instrument is the Mastersizer 3000E (MS3000E) by Malvern, which applies a technique similar to the LISST, but with more precision, range, accuracy and efficiency. First the collected samples were added to an included mixer containing freshwater that is feeds into the instrument. The mixer makes the dilution homogeneous and delivers volumes into a laser cell of the instrument. Similar to the LISST, laser light is transmitted and diffracted into bins. The results are stored into a connected PC with a user interface for analyzing multiple consecutive samples and outputs with the raw particle size data, automatic GSD plots, estimated volumetric sediment concentration and various other properties. A screen-capture image illustrating the output of this device is given in Figure 19.

The grain-size results of the MS3000E were compared to those of the LISST and those of known control standard samples. The results of the MS3000E were far more accurate and precise when compared to the standards, therefore the grain-size results for all of the samples are taken from the MS3000E. More specifically, samples initially analyzed with the LISST were also re-analyzed with the MS3000E. The concentration results of the MS3000E were compared to concentration results of the weighing method and to those of control standard samples. The concentration results of the MS3000E compared well to the control standards and to the weighing method. Due to the pace at which concentrations can be measured, all concentration results reported here were taken from the MS3000E, with the use of the weighing method retained a secondary comparison for some samples.

$$C\% = \frac{V_s}{V_s + V_w} \times 100\% \tag{13}$$

3 Figures for Section Experimental Methods

This section includes only the figures that are referenced in Section 2 'Experimental Methods'. Other figures may be found in separate sections following the sections in which they are referenced.

Figure 1: Photograph of the Garcia Density Current Tank at Hydrosystems Laboratory, University of Illinois, used in the experiments. View is from upstream to downstream progressing from left to right and section labeling convention used in Greek letters from $\alpha - \zeta$. A large damping tank can be seen at the downstream end.

Figure 2: Mixing tank with propeller, pump setup, and piping used for creating and delivering the sediment slurries.

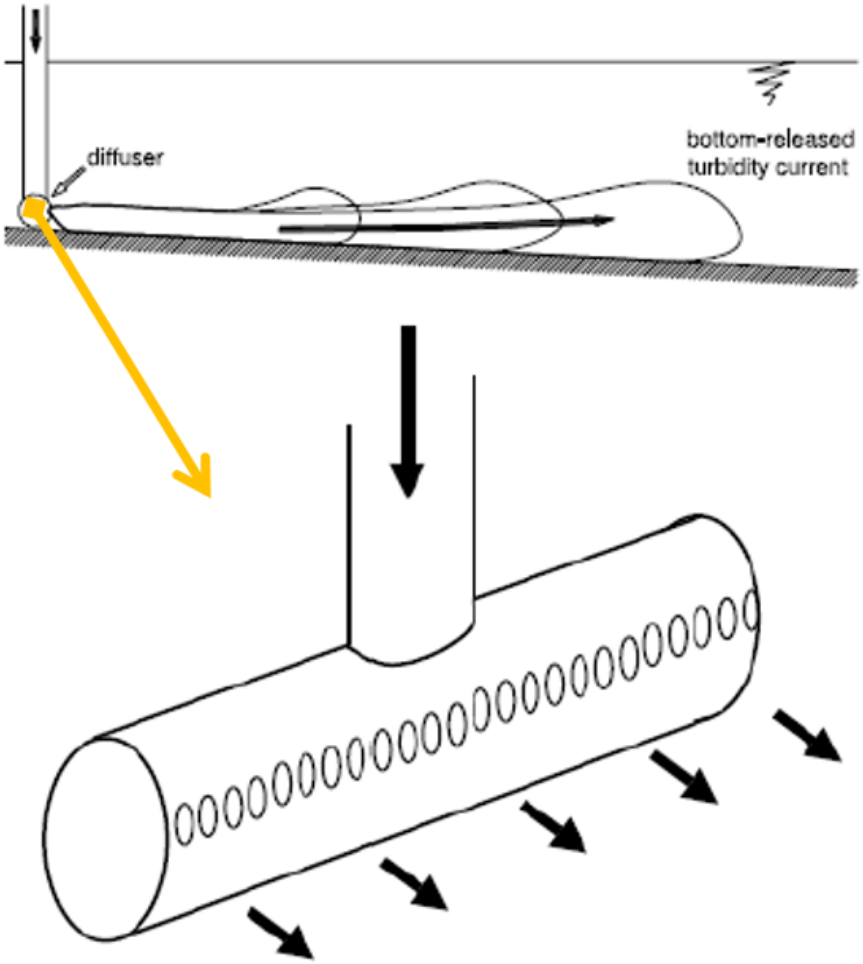

Figure 3: Diagram of input mechanism and slurry diffuser for the experiments; originally from Sequeiros et al. (2009).

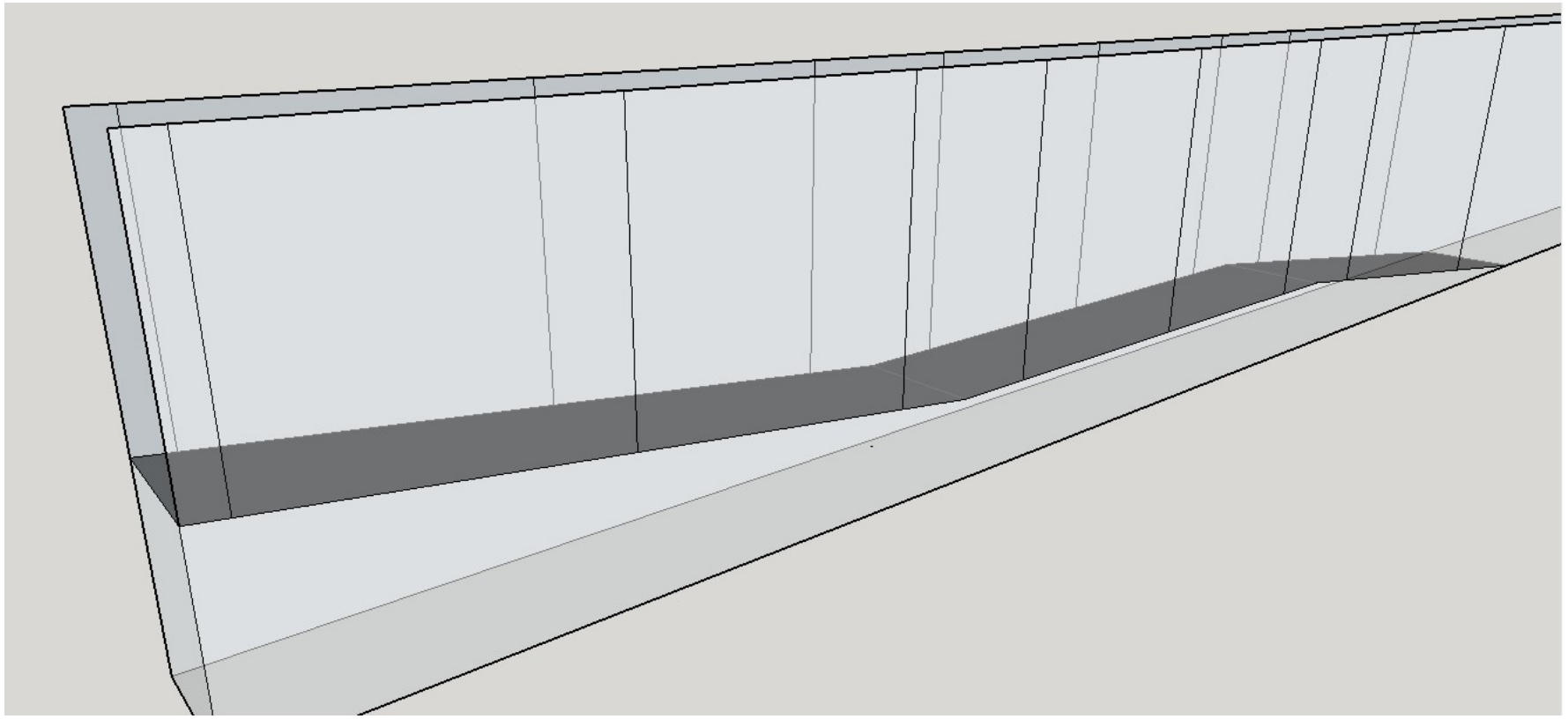

Figure 4: 3D drawing of the original bed configuration for the first set of experiments.

Figure 5: Photograph of the original bed configuration for the first set of experiments.

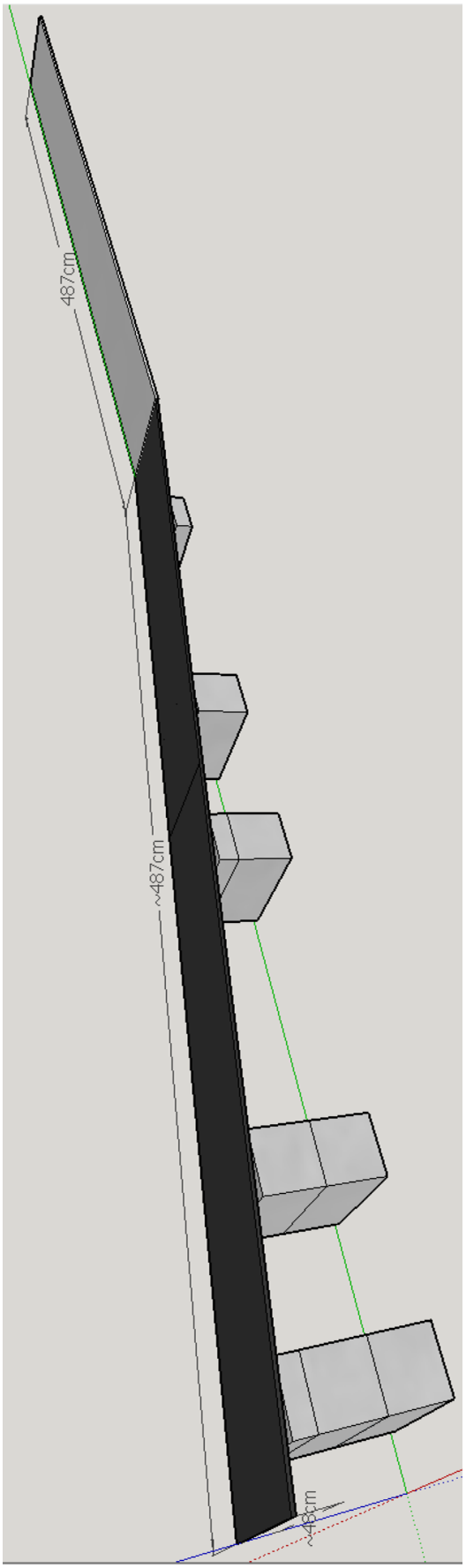

Figure 6: 3D drawing of the final slope configuration used in the experiments.

EPK Clay

Description: EPK Kaolin is a unique, high quality, water washed, ceramic kaolin which offers very white fired color, unusually good forming characteristics and high green strength. In glazes, EPK offers excellent suspension capabilities and uncommon cleanliness.

Typical Analysis

Chemical Analysis:	SiO_2	45.73%	CaO	0.18
	Al_2O_3	37.36	Mgo	0.098
	Fe_2O_3	0.79	Na_2O	0.059
	TiO_2	0.37	K_20	0.33
	P_2O_5	0.236	LOI	13.91

Mineral Content (X-Ray Diffraction):	Kaolinite (Al_2O_3, $2SiO_2$, $2H_2O$) - 97%
Screen Residue(Water washed through screen):	Pellet (Prill): .339 +325 mesh Airfloated: .245 +325 mesh
Specific Surface Area (m^2/g):	28.52
Median Particle Size (Microns):	1.36
Free Moisture:	Pellet (Prill) 3.0% Airfloated 1.0%

Ceramic Properties

pH (10% Solids-Wt.):	5.8
Viscosity:	10,000 CPS @ 35% solids (wt.)
Water of Plasticity:	26.0%
Dry Modulus of Rapture	300 psi
Linear Dry Shrinkage:	5.8%
Fired Shrinkage Cone 11: (1315°C)	11.6%
Absorption - Cone 11: (1315°C)	11.3%
Cation Exchange Capacity (Methylene Blue Index):	4.5 meq./ 100 grams
Fired Color (100% Clay, Cone 11):	95.1

Figure 7: Manufacturer's list of sediment properties for the Edgar Plastic Kaolin kaolin clay used as a mud surrogate in the experiments.

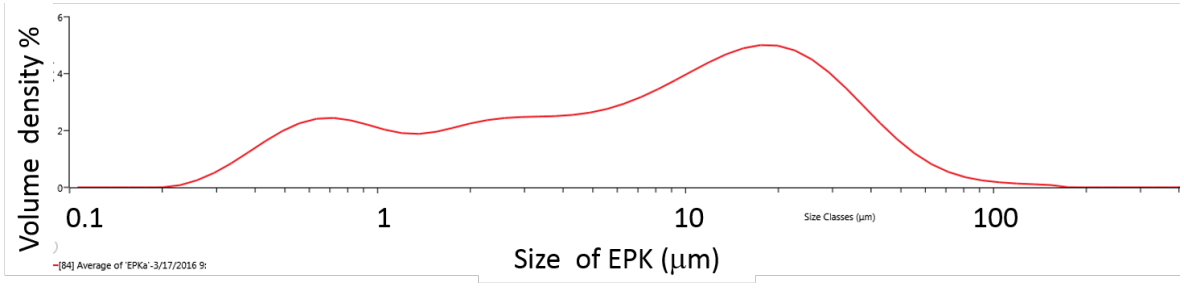

Figure 8: Grain-size distribution of the raw EPK kaolin clay sediment as determined from the Mastersizer 3000E particle sizer, without the use of ultrasonic dispersion.

SIL-CO-SIL® 250

GROUND SILICA

PLANT: OTTAWA, ILLINOIS

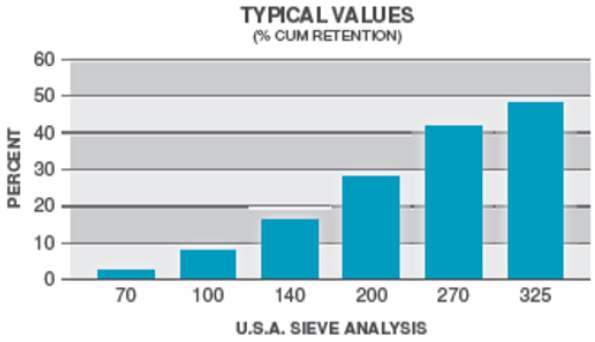

USA STD SIEVE SIZE		TYPICAL VALUES		
		% RETAINED		% PASSING
MESH	MICRONS	INDIVIDUAL	CUMULATIVE	CUMULATIVE
70	212	2.7	2.7	97.3
100	150	5.4	8.1	91.9
140	106	8.0	16.1	83.9
200	75	11.9	28.0	72.0
270	53	13.5	41.5	58.5
325	45	6.4	47.9	52.1

TYPICAL PHYSICAL PROPERTIES	
Hardness (Mohs)	7
Melting Point (Degrees F)	3100
Mineral	Quartz
pH	7
Reflectance (%)	78
Yellowness Index	4.8
Specific Gravity	2.65

TYPICAL CHEMICAL ANALYSIS, %	
SiO_2 (Silicon Dioxide)	99.7
Fe_2O_3 (Iron Oxide)	0.0217
Al_2O_3 (Aluminum Oxide)	0.123
TiO_2 (Titanium Dioxide)	0.0096
CaO (Calcium Oxide)	0.0096
MgO (Magnesium Oxide)	<0.01
Na_2O (Sodium Oxide)	<0.01
K_2O (Potassium Oxide)	0.02
LOI (Loss On Ignition)	0.1

May 21, 2018

Figure 9: Manufacturer's list of sediment properties for the Sil-Co-Sil 250 used as a sand surrogate in the experiments.

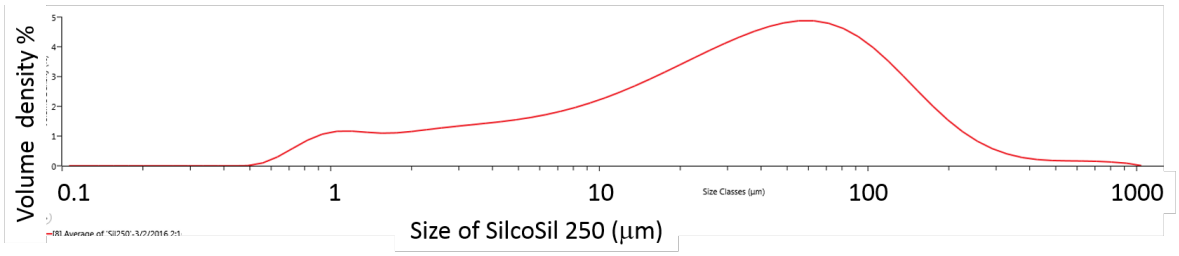

Figure 10: Grain-size distribution of the raw Sil-Co-Sil sediment as determined from the Mastersizer 3000E particle sizer, without the use of ultrasonic dispersion.

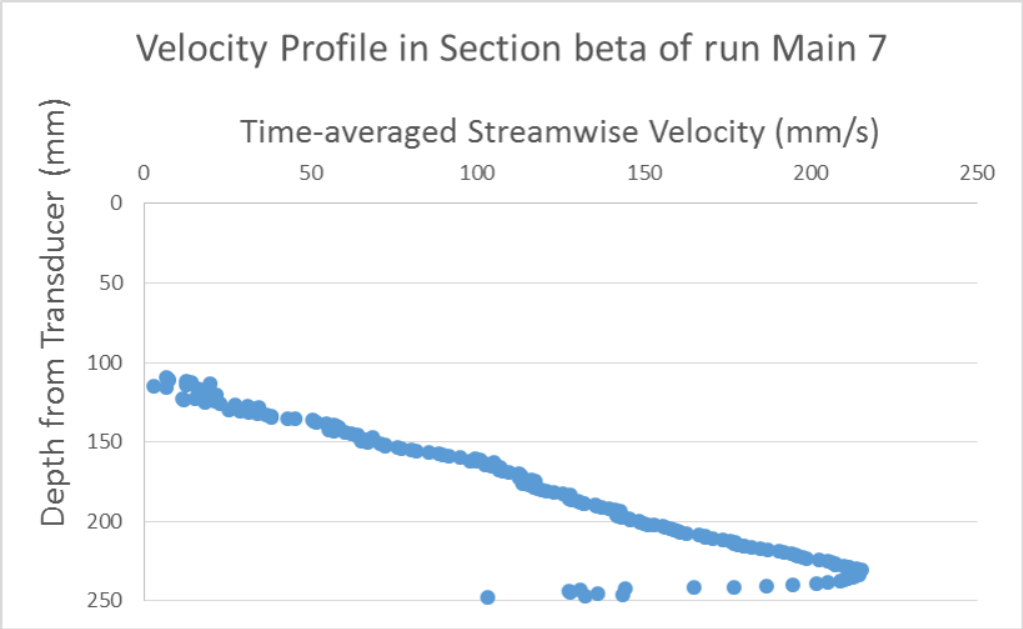

Figure 11: Velocity profile obtained from UVP measurements in section beta (see Figure 1) of run Main 7 with a relatively dilute total sediment concentration of 3% by volume. The profile was collected on the sloped end of the tank and is presented here at the same scale as Figure 12.

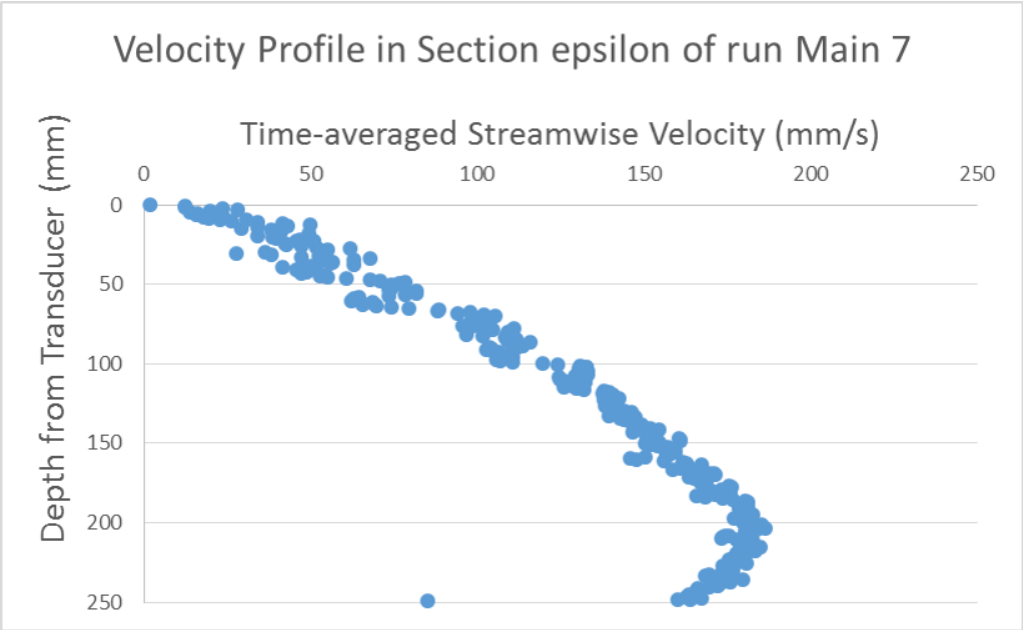

Figure 12: Velocity profile obtained from UVP measurements in section epsilon (see Figure 1) of run Main 7 with a relatively dilute total sediment concentration of 3% by volume. The profile was collected on the horizontal end of the tank, and is presented here the same scale as that of Figure 11.

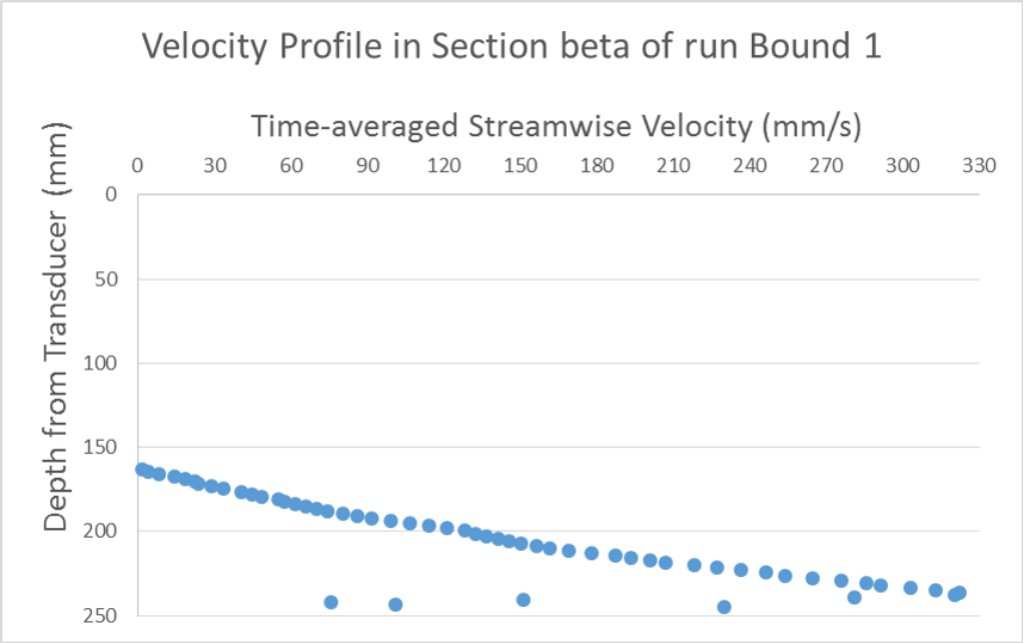

Figure 13: Velocity profile obtained from UVP measurements in section beta (See Figure 1) of run Bound 1 with a relatively high-concentration of total sediment of 20% by volume. The profile was collected on the sloped end of the tank and is presented here at the same scale as that of Figure 14.

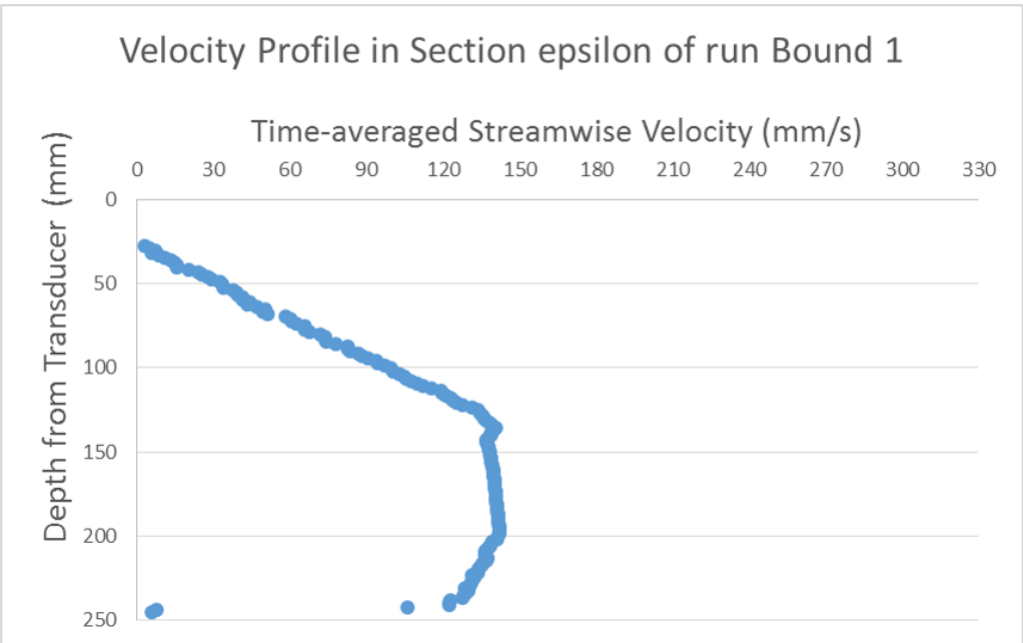

Figure 14: Velocity profile obtained from UVP measurements in section epsilon (Figure 1) of run Bound 1 with a relatively high-concentration of total sediment of 20% by volume. The profile was collected on the horizontal end of the tank and is presented here at the same scale as that of Figure 13.

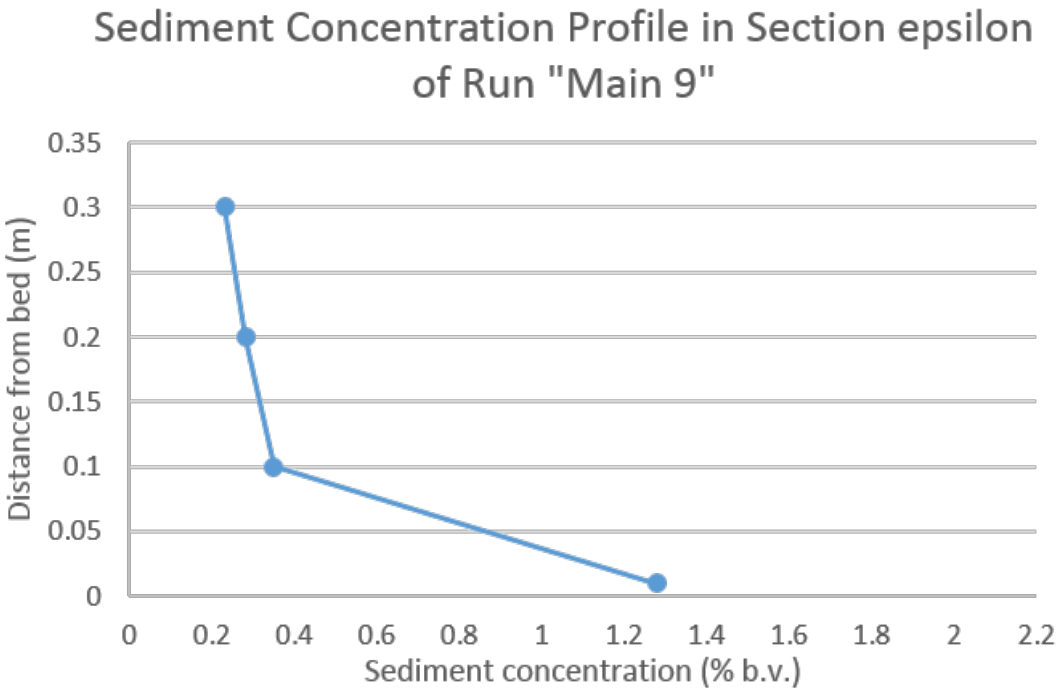

Figure 15: Example of an upward-normal sediment concentration profile of a transitional flow from run Main 9. The profile represents the volumetric sediment concentrations collected in section epsilon which is downstream of the slope break in the tank.

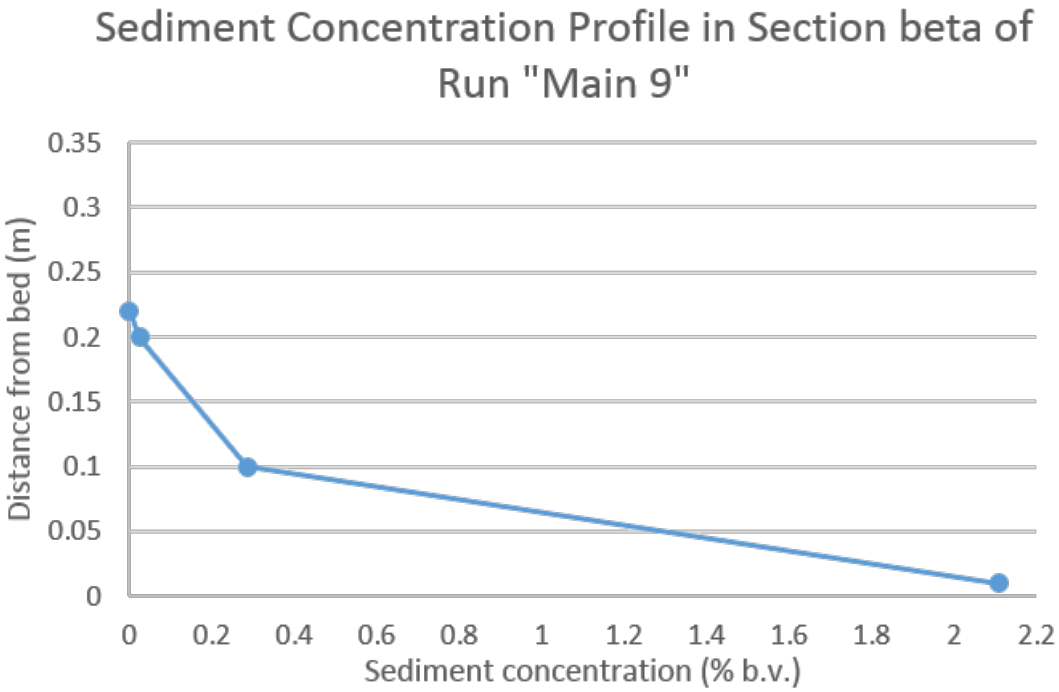

Figure 16: Example of an upward-normal sediment concentration profile of a transitional flow from run Main 9. The profile represents the volumetric sediment concentrations collected in section beta which is on the slope of the tank.

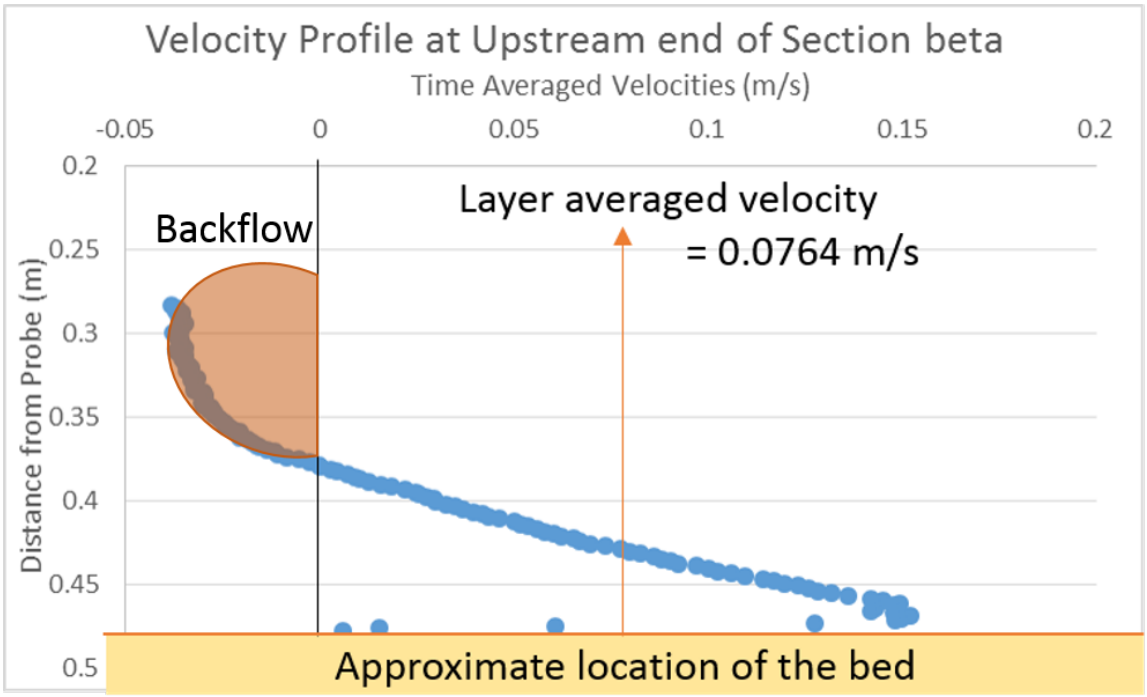

Figure 17: Example of velocity profile during run Main 1 in section beta obtained by the UVP. A diagram for overlain on the profile labels the location of the bed, backflow, and layer averaged velocity.

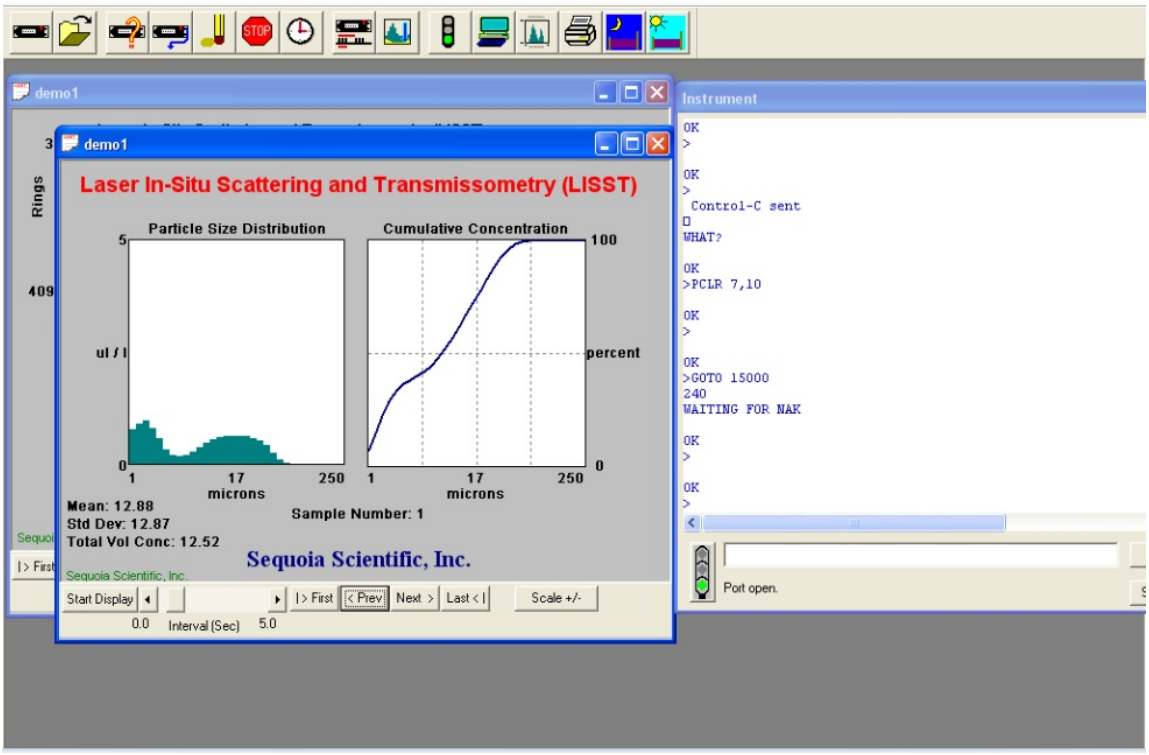

Figure 18: Screen capture image from the PC software for the LISST showing the user interface and an example grain-size distribution in the left plot and cumulative size distribution in the right.

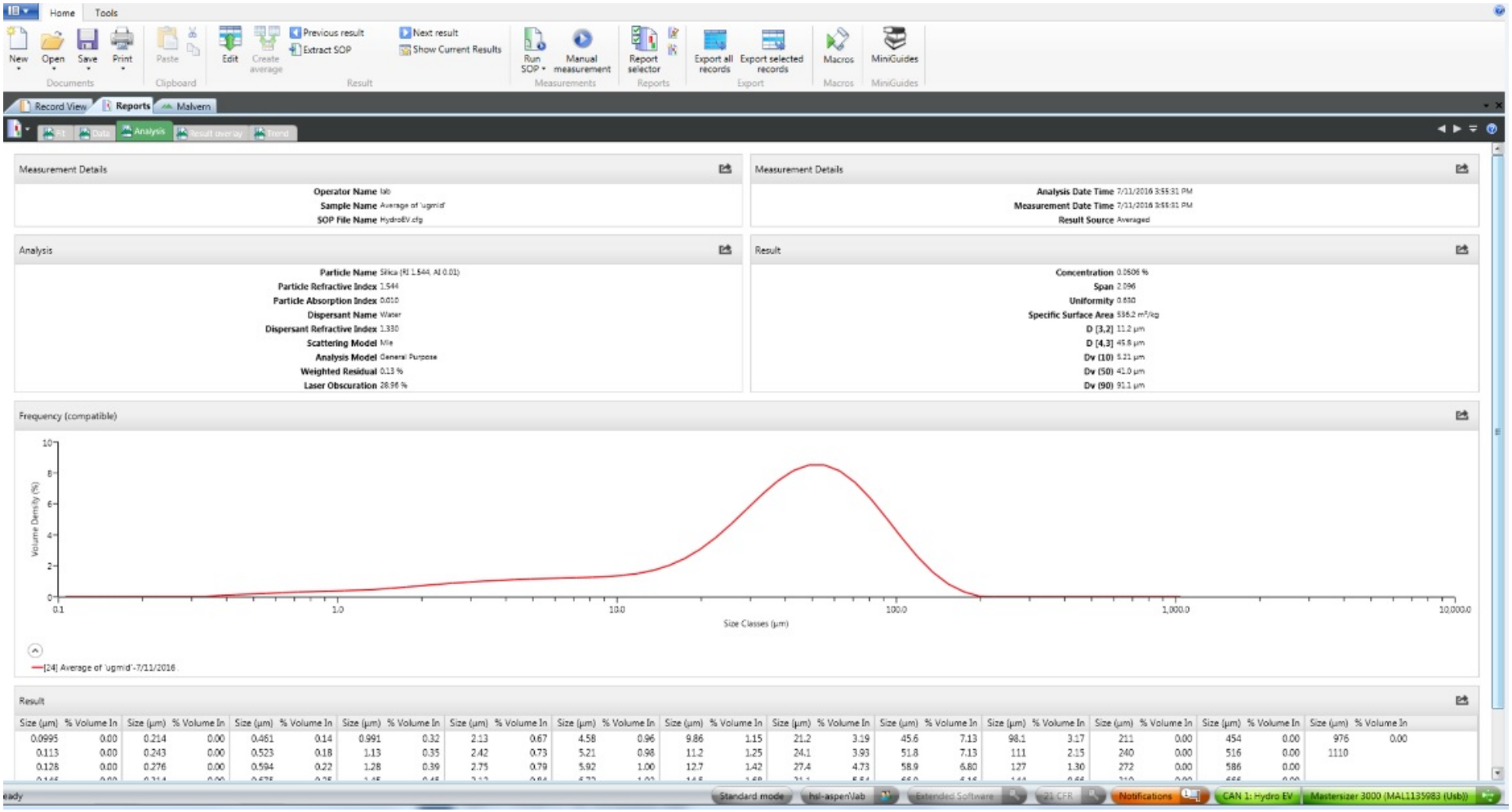

Figure 19: Screen capture image from the Mastersizer 3000E instrument software. Figure shows analysis display where the results including a table and plot of GSD for a sample measurement.

4 Result of Experiments

The experiments conducted have been composed of flows in the transitional regime between turbidity currents and submarine debris flow, using criteria suggested in previous literature. The first few experiments had limit measurements because they were exploratory runs where parameters were adjusted until the flows were determined to be with the transitional regime. For the adjustments the initial slope and slurry input parameters such as discharge were increased in increments. A slope of about 7° and input slurry flow rate of about $1.0L/s$ achieve flow results in the transitional regime flows for the flume. As previously stated the transitional regime was determined by the range of Reynolds number found by Baas in 2009. After the first exploratory runs, measurements of the bed were included to determine that the runs resulted in deposits that were consistent with HEBs. After the exploratory runs it was ensured that flow velocity, concentration, and bed measurements were recorded for all experiments including those where deposits of HEBs were obtained.

A total of 43 experiments have been conducted. In each of the runs at least two sections of the flume upstream of the slope break as well as at least two sections downstream have measurements of all of the following: flow geometry, flow velocities, sediment concentrations of the flow, sediment GSDs in the flow, bed geometry, bed evolution, and bed sample GSDs. 14 of the runs were conducted in a smaller scale flume that was used to collect the exploratory results during an early period when the main density current tank was undergoing repairs and pump renovations. The main set of experiments have been focused on argillaceous-type HEBs, i.e. those emplacing a mixture of grain sizes and/or a mixture of silica and kaolin, so as to quantify the flow characteristics and deposits that are associated with various content fractions of fine-grain sediment. The flow measurements of profiles upstream, above, and downstream of such deposits also allow us to determine the flow conditions that emplace HEBs.

4.1 Data

All of the data from measurements in the experiments are organized in the table included in Appendix B. The 'Run ID' column lists the name given to each experimental run; these are used to organize the runs. The column 'UVPfile' indicates the name given to each measurement file from the UVP during each run. The 'Location' column identifies where along the flume the corresponding measurements were taken. The 'H (cm)' column gives the thickness of the resulting deposit from that run in centimeters. The 'L (cm)' column gives the location of the measurements as a distance from the inlet diffuser at the upstream end. The 'Kaolin%' column gives the found percent of the total grains that is kaolin grains as specified in Eq. 12. The 'AC%' columns give the relative percentage of fine grains as specified in Eq. 11 found within the corresponding deposit. The 'U (m/s)' column are the results of the layer-averaged velocity for each location in meters per second. The 'C (m^3/m^3)' column are the results of the flux-averaged volumetric concentration found for the flow at each location. The 'C_o (m^3/m^3)' column are the volumetric concentration of the inflow for each run. Lastly, the 'Re #' and 'Fr #' column respectively are the resulting Reynolds number and densimetric Froude number for the density currents as computed from Eq. 1 and Eq. 6, respectively.

Many of the experiments were conducted over antecedent deposits to determine bed evolution and morphology, with the exception of runs where the Run IDs are marked with an asterisk, e.g. '*Main1' in the Appendix B. The asterisk specifies which of the runs were conducted over the bare bottom of the flume. It is important to note that the runs were conducted in a specific order. In each experiment where the bed was not cleared, runs with the greatest total sediment concentration input were run prior to others. Runs with greater input concentrations of silica also had priority. This was because the runs with higher sediment concentration may rework antecedent deposits more readily. The generally finer deposits of the kaolin also may become re-entrained more easily which is why the runs with more silica were usually conducted first. There were some exploratory runs where the bed was allowed to become reworked and measurements were taken.

4.2 Transitional Flow Characteristics

The experiments conducted to date cover a range of flow regimes, but with emphasis on those flows in the transitional regime as suggested in previous work. The experiments included transitional flows which range from turbulence-enhanced transitional flow (TETF), lower transitional plug flow (LTPF), upper transitional plug flow (UTPF), and quasi-laminar plug flow (QLPF) as defined by Baas et al. (2011). A continuation of the experiments is suggested to cover a range of flows expected to have turbulence both further increased, and more suppressed; this may involve adjusting inflow rate as well as input concentrations as discussed later.

A short clip of a video recorded during one of the runs with a transitional regime flow is presented in the Annex file under Video 1. The video may help illustrate how a transitional regime flows appears and evolves. From the clip it may be seen that the density current in the video shows a fairly sharp lutocline, suggesting that the flow is not fully turbulent there. On closer inspection there is some mixing at the interface of the flow and the ambient water, though suppressed, which implies that the flow is not quasi-laminar either, but may be within a transitional regime for turbulence. Analysis of the Reynolds number using Eq. 1 from the data corresponding to the flow in the video confirms that the flow is indeed in the LTPF regime. The video also illustrates one location where measurements of both velocity and concentration were being collected for such analysis. Another example of such measurement area may be seen in the labeled photograph in Figure 20.

Dimensionless parameters were computed with the measured flow properties. Dimensionless numbers help to compare the rheological results with the results of other experiments in laboratory physical models that pertain to sediment density currents. The particular dimensionless numbers of interest are the previously described Reynolds number for turbulence from Eq. 1 and the Richardson number characterizing mixing from Eq. 5. Dimensionless parameters are of interest because they may be applied to any scale or experimental setup, and thus allow comparison with other related experi-

ments. For the comparison, the data from our results is plotted together with those in the experiments of Baas et al. (2011) in Figure 21. The figure shows a phase diagram experimental results that emplaced HEBs with Re on the vertical axis and Frd on the horizontal axis.

As displayed in Figure 21, the results of Baas et al. (2011) are presented as the colored data points. They serve to designate the spectrum from turbulent flow on the top through transitional regimes to quasi-laminar flow on the bottom. The data points plotted in black diamonds are the results from the current project. Another addition is the straight purple line on the bottom left corner which represents the boundary where kaolin deposits out completely. Figure 21 is only intended to serve as a guideline to show the runs conducted are along the range of flows found to be transitional regime sediment density currents. Looking toward the future more experiments could be conducted to compliment the results of the previous runs with parameters that further increase and/or further reduce turbulence in order to better understand how transitional flows with relatively higher or lower Re influence their corresponding sedimentary patterns for comparison.

4.3 Sediment Transport and Deposition Patterns

When running experimental sediment density currents within the transitional flow regime it was determined that the deposits indeed had signatures of the types of HEBs. The sediment bed deposits were sampled and analyzed in order to be identified as HEBs or any other depositional structure of interest. For all of the runs the MS3000E sediment analysis resulted in GSDs with coarser tails for deposits near the diffuser and GSDs with finer tails further downstream in general. The pattern may be due to preferential settling of courser grains. Much coarser sands were often found within alpha, the upstream most section, which may be due to grains that settle out in proximity to the jet caused by the input diffuser dissipates. The downstream fining result tends to be especially rapid downstream of the slope break where fines show up in the sediment GSDs in relatively more abundance.

Quantities of argillaceous content Ac as in Eq. 11 as well as the relative content of kaolin and silica was determined for multiple streamwise locations in the various runs. The results include a spectrum of deposits that may be considered surrogates for cleaner sand to argillaceous sands to debrite. Many runs had locations with bed sample measurements, e.g. the GSDs in Figure 22 - Figure 24, showing the sediment in the deposits having significant volumes of fines which may reference beds considered significantly argillaceous when comparing to deposits in the field. Bed sample measurements in other locations or in other runs, e.g. the GSDs in Figure 25 - Figure 27, the deposits contained mostly coarser grains which may reference beds considered as cleaner sands when comparing to deposits in the field. The plots shown are just a few of the hundreds of GSDs results recorded for bed samples during the runs. With the deposits containing kaolin, the kaolin grains in the samples tend to form some amount of aggregates or flocs that may act as larger grains. Such samples had GSD obtained both with the composite grains and their constituent grains quantified with the use of ultrasonic dispersion as discussed below.

The properties of the sediment source is important in sediment density current research. Figure 28 is a plot of GSD for the parent material of the silica and the kaolin overlain. Figure 29 is a GSD plot for an example sediment mixture composed of silica 50% by weight and kaolin 50% by weight. It may be seen that the GSD results have a more bimodal distribution corresponding to the peak from median kaolin size and peak from median silica size. A deposit with a GSD having signature of a mode in the kaolin size range and a mode in the silica size range is evidence that the bed contains the both the kaolin and the silica. It is imperative to note that the GSD results in Figure 28 and Figure 29 are of samples that underwent ultrasonic dispersion in the MS3000E instrument. Ultrasonic dispersion is discussed in greater detail below.

The MS3000E has a mode of measurement with pulsing of ultrasonic frequencies. The frequencies break up aggregates and flocs in a sample in a process referred to as ultrasonic dispersion. Grain-sizing with the MS3000E is conducted twice; analysis first without ultrasound and then with ultrasound. A comparison of the GSDs obtained both with and without ultrasound dispersion shows a shift in GSD as indicated in Figure 30.

Only the kaolin can form composite particles so the result also allows for an indirect indication of the fraction of kaolin in the sample. Even deposits with relatively low volumes of kaolin still showed evidence of aggregates or flocs. It is important to note that although the composite particles may deposit as coarser grain material like the silica, the post-depositional nature of the kaolin, such as influence on permeability and reservoir potential, may be far different from equivalent-sized silica material. This issue deserves attention in its own right.

It is important to note that the kaolin sediment is brown in color especially in comparison to the silica which is bright white. Using visual discrimination it may be seen that the silica and kaolin can indeed deposit together because the deposits emplaced by the different runs have various shades of brown-to-white depending on the relative content of kaolin or silica respectively. Deposits with more kaolin (browner coloration) or more silica (whiter coloration) may be compared in the streamwise profile photograph of Figure 31 and cross-section photograph of Figure 32. The results of the project relies on the importance of determining relationships between the rheology and the content of kaolin relative to the silica and also such relationship between the content of fines A_c (Eq. 11).

Another method used to help quantify the contents of the deposits was a scanning electron microscope (SEM). The SEM was used in a few cases to count grains in images such as Figure 33. The grains sizes may be estimated by comparing with the scale included and an approximation of Ac is determined and compared to the results of Ac from the MS3000E. The SEM also has x-ray analysis which can be used to discriminate between a silica particle and a kaolin particle to find Kc (Eq. 12). More specifically, x-ray analysis can predict the presence of aluminum which is diagnostic of kaolin. The SEM is not used in most cases because it requires depressurization of the sample, which cannot be done if the sample has water content. This was particularly a problem for the deposits with higher kaolin content. The SEM results were primarily used to confirm grain-size and grain type results that had been determined with the previously described methods. The results of imaging from the SEM are considered as a standard for the previous methods

of sediment type quantification.

Deposits that did not fit the paradigm of an HEB, but which had of interesting depositional patterns or structures were also noted and studied. For most runs, small bedforms tend to develop on or near the sloped portion of the flume (i.e. sections alpha and beta, and the updip half of section gamma in Figure 1). The bedforms may be seen in plan view as in the bed of Figure 34 and in profile view as in the depositional patterns seen in Figure 35. It was determined that the relatively high velocities in such locations, i.e. proximal to the diffuser and slopes, have enough bed shear stress and bedload to create downstream-migrating bedforms. When running over preceding deposits the flow may interact with the bed, in particular with bedforms because the bed was only cleared or reworked in certain runs as specified in Appendix B.

5 Figures for Section Results of Experiments

This section includes only the figures that are referenced in Section 4 'Results of Experiments'. Other figures may be found in separate sections following the sections in which they are referenced.

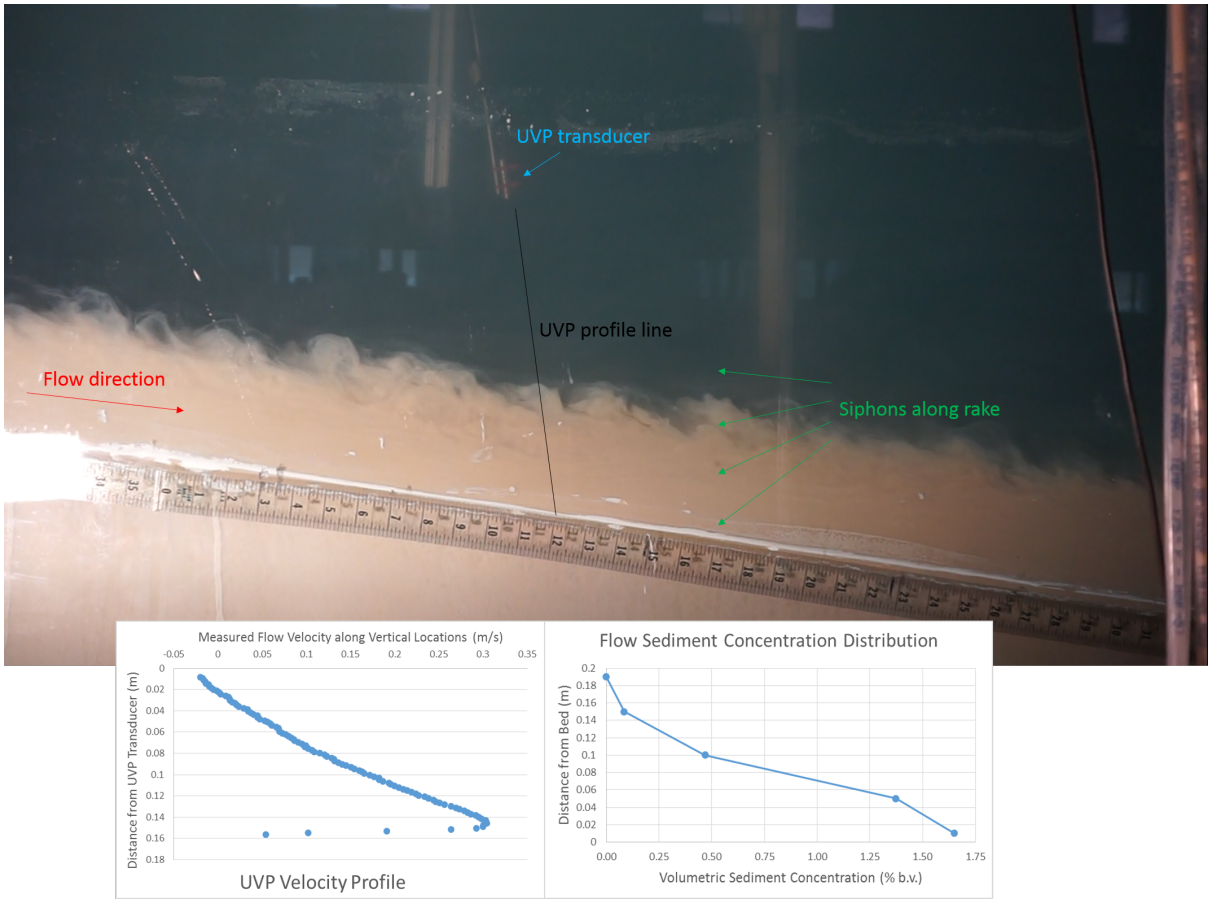

Figure 20: Photograph of section beta during run Bound 4 when measurements were being collected. A notarized overlay identifies key items in the photograph. Two plots below display the resulting velocity profile (left) and resulting sediment concentration profile (right) of the flow.

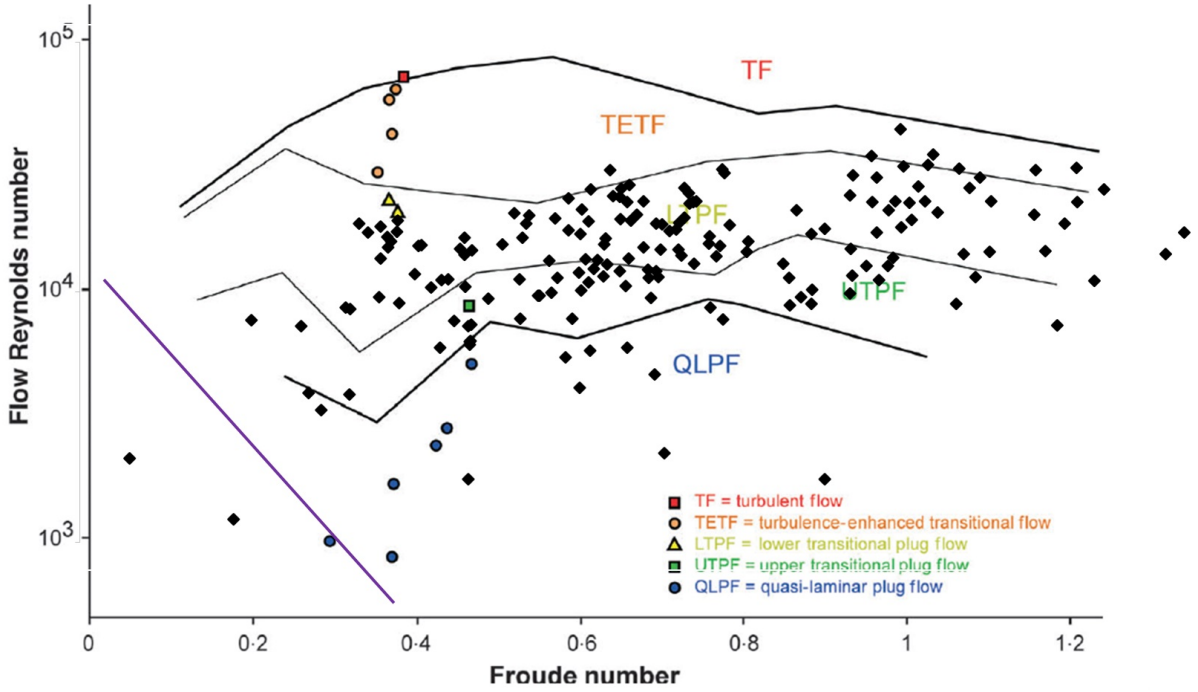

Figure 21: Phase diagram of transitional kaolin silica mixture flow with select experimental data from Baas et al. (2011) (colored data points) with results of our experiments (black, diamond-shaped data points). Solid black lines separate flow types designated, as designated in Baas et al. (2011). Solid purple line identifies the approximate location where all kaolin is deposited out.

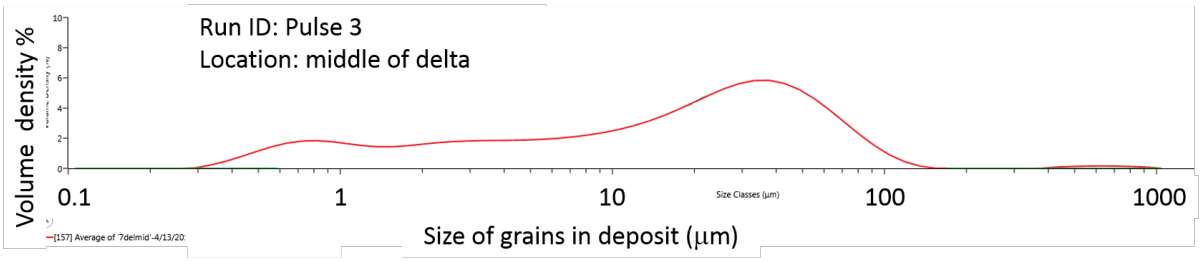

Figure 22: Grain-size distribution of bed material sample after run Pulse 3 in section delta (see Figure 1). Represents an experiment with deposit results of relatively large value of Ac. Figure 22 - Figure 27 are all plotted on the same scale.

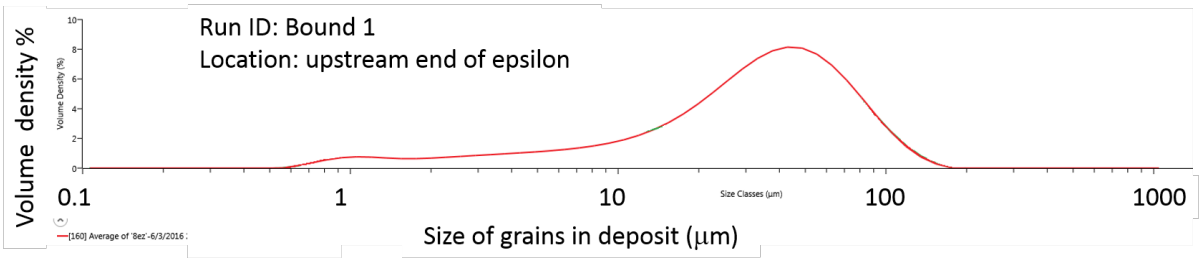

Figure 23: Grain-size distribution of bed material sample after run Bound 1 in section epsilon (see Figure 1). Represents an experiment with deposit results of relatively large value of Ac. Figure 22 - Figure 27 are all plotted on the same scale.

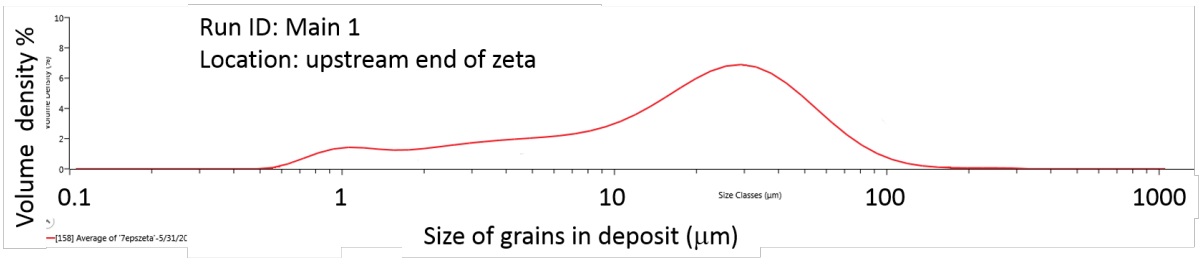

Figure 24: Grain-size distribution of bed material sample after run Main 1 in section zeta (see Figure 1). Represents an experiment with deposit results of relatively large value of Ac. Figure 22 - Figure 27 are all plotted on the same scale.

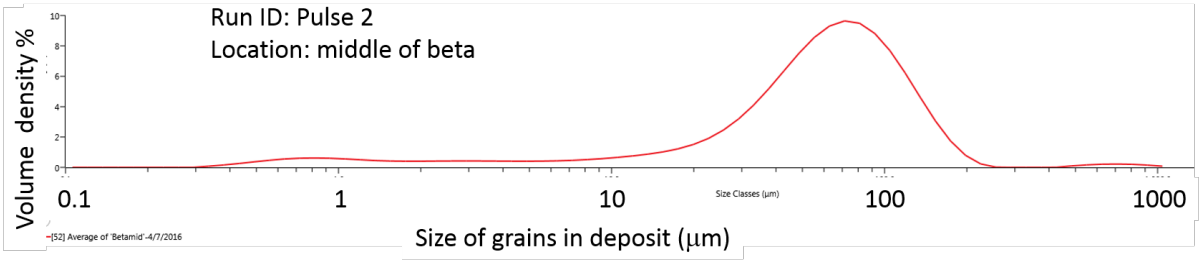

Figure 25: Grain-size distribution of bed material sample after run Pulse 2 in section beta (see Figure 1). Represents an experiment with deposit results of relatively large value of Ac. Figure 22 - Figure 27 are all plotted on the same scale.

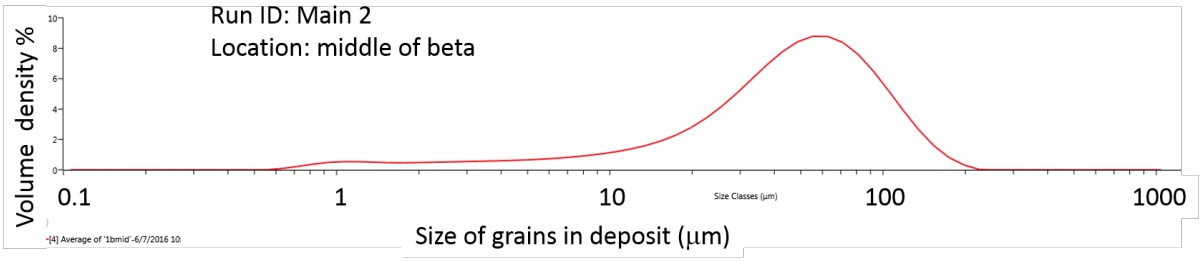

Figure 26: Grain-size distribution of bed material sample after run Main 2 in section beta (see Figure 1). Represents an experiment with deposit results of relatively large value of Ac. Figure 22 - Figure 27 are all plotted on the same scale.

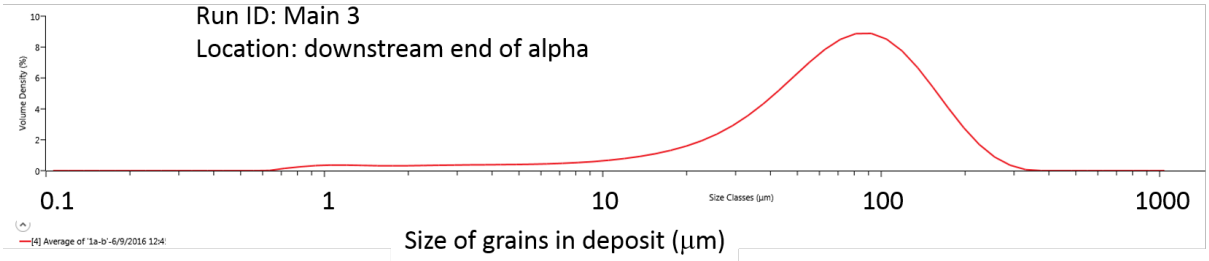

Figure 27: Grain-size distribution of bed material sample after run Main 3 in section alpha(see Figure 1). Represents an experiment with deposit results of relatively large value of Ac. Figure 22 - Figure 27 are all plotted on the same scale.

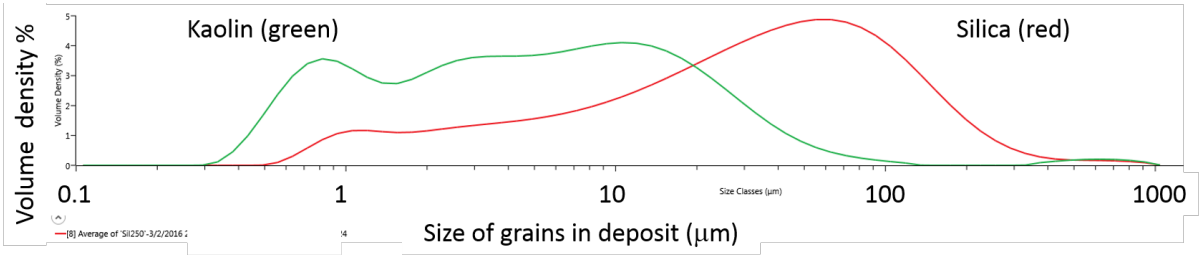

Figure 28: GSD of the sediment parent material used in the experiments. Raw kaolin in green and the raw silica in red.

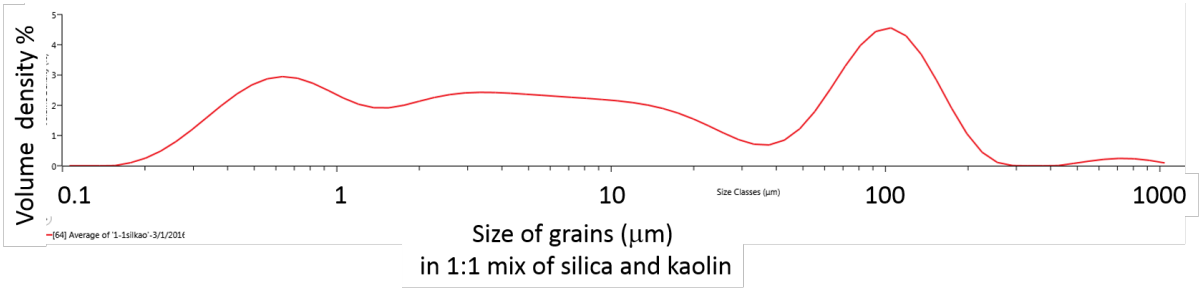

Figure 29: GSD of a sample composed of 50% kaolin and 50% silica by weight. The results of the GSD are those taken after the sample underwent ultrasonic dispersion to breakup aggregates and flocs.

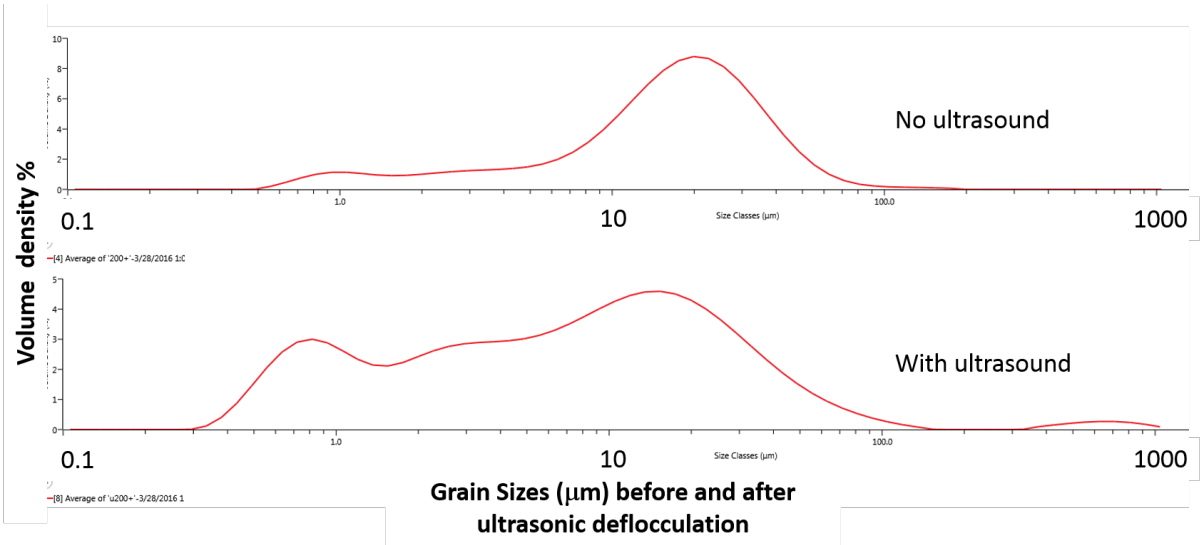

Figure 30: grain-size distributions of a bed sample, the top being before ultrasonic dispersion, and the bottom after ultrasonic dispersion. Note the relative increase in content toward the finer end in the top plot, as compared to the bottom plot.

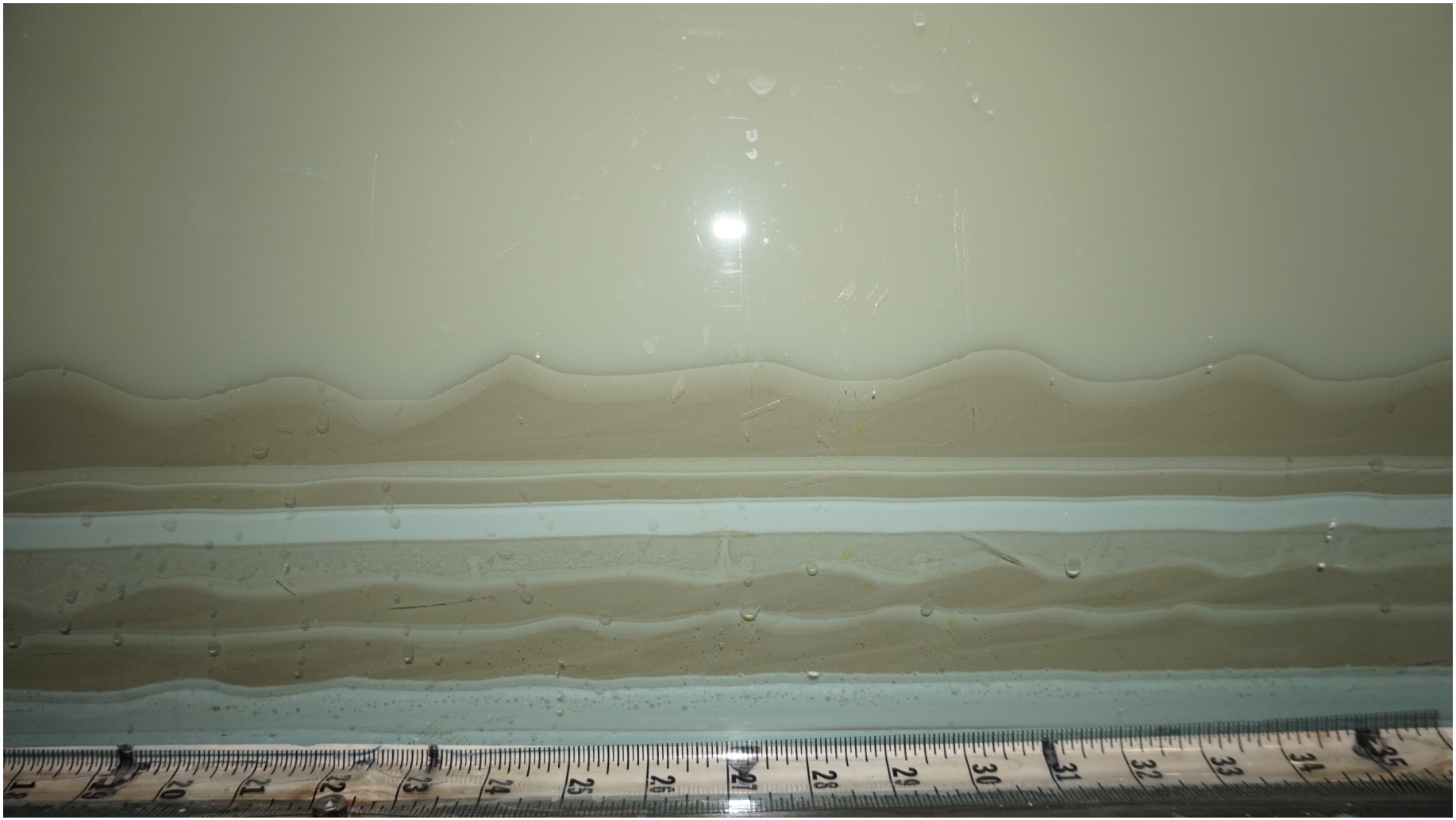

Figure 31: Photograph of deposits in section gamma after a series of seven runs. Image displays the contrasting deposit colors and shadings do to variable kaolin content. Note other features of interest including bedforms and striations.

Figure 32: Photograph of deposit in section beta after one exploratory run. Image displays the contrasting deposit colors and shading due to variable kaolin content. The bare flume may be seen exposed on the bottom with the grey color.

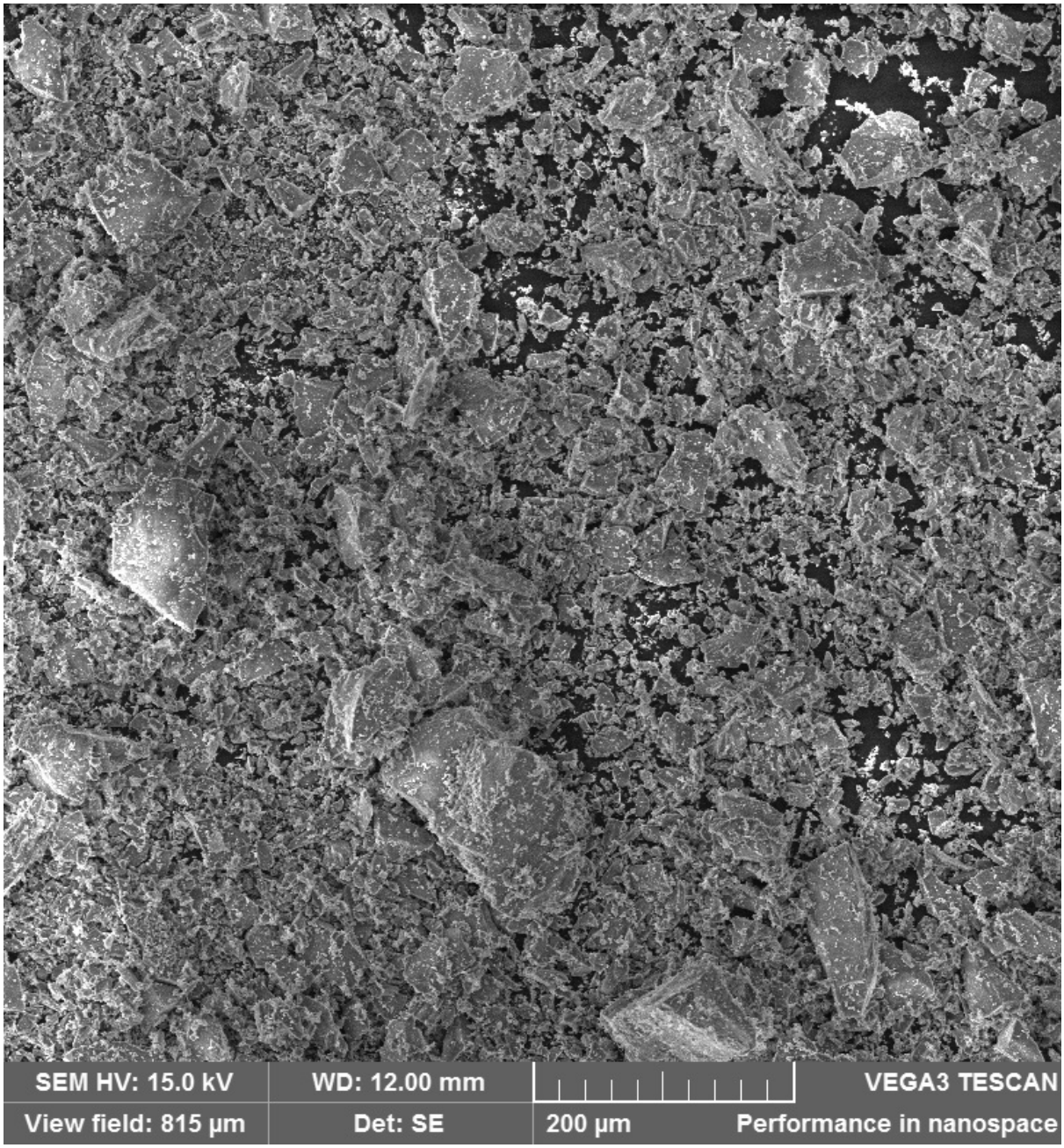

Figure 33: Photograph from the Scanning Electron Microscope imaging a mixture of 50% silica flour and 50% kaolin by weight.

Figure 34: Plan view of 180 cm reach corresponding to sections alpha and beta (in left to right streamwise direction) of the bed after the experiment Explore 2. The slope of the bed is 7 degrees. Two-dimensional bedforms with may be seen.

Figure 35: Profile view of 76-cm reach in section gamma with no slope and left to right streamwise direction. There are stacked deposits from runs Main 1, Bound 2, Main 2, Main 3, and Main 4 from bottom to top respectively. Bedforms from the high-concentration run Bound 2 may be seen. The darker zones correspond to relatively coarse deposits. The lighter layers are the settling caps from the very fine-grained material coming out of suspension over days.

6 Discussion and Direction

Focus was put on determination of the content of kaolin K_c and content of fines A_c in the matrix of the resulting deposit. The results for K_c and A_c are numerical properties of the deposit that were used to explore for relations amongst the multiple flow properties pertaining to rheology, as hypothesized. When considering the results of all of our runs with the various input slurry kaolin-silica compositions we find that: A_c is independent of the Richardson number alone; A_c is independent on the flux-averaged concentration alone; A_c has almost no dependence on the Reynolds number alone as in Figure 36; A_c has almost no dependence on the layer-averaged velocity alone; A_c has almost no dependence on the input sediment concentration alone; A_c has a tendency to increase with downstream distance; A_c has weak inverse relation to deposit thickness as in Figure 37 which is labelled by runs with different input slurry sediment concentration C_o. The deposit thickness H of Figure 37 is made dimensionless as H^* in Eq. 14 by dividing it by the upper limit of the argillaceous grain diameter of $D_a = 11.2$ microns.

$$H^* = \frac{H}{D_a} \tag{14}$$

Again when considering the results of all of our runs with the various input slurry kaolin-silica composition: K_c is independent on the Reynolds number alone; K_c is independent on the Richardson number alone; K_c is independent on the layer-averaged velocity alone; K_c is independent on the flux-averaged velocity alone; K_c is independent on the inflow slurry sediment concentration alone; K_c tends to increase with downstream distance; Kc has some dependence on the kaolin composition of input sediment slurry. The kaolin composition of the inflow slurry is defined by the concentration of kaolin in the inflow slurry K_o divided by the inflow slurry total sediment concentration C_o and most of the dependence of K_c on K_o comes from runs where the inflow slurry had no kaolin and so the deposits also had no kaolin, and also runs where the sediment in the inflow slurry was solely kaolin, so that the deposits were also completely kaolin.

There are also connections between the properties of the flows and properties of the deposits that may not be evident by comparing single factors of the flows and deposits. There are stronger correlations between the flow properties and deposit properties when looking at argillaceous content factored with deposit thickness i.e. effective argillaceous thickness $A_c H^*$ in Eq. 15. The physical meaning of argillaceous thickness is a dimensionless height of the argillaceous deposit in grain diameters as taken by the upper bound for A_c. This parameter may be important when comparing results with field observations and computer models. As seen in the plots of Figure 38 and Figure 39 argillaceous thickness is dependent on not just concentration, but also the composition of the sediment of the inflow slurry. From the results seen in Figure 38 there is the trend such that when the flows have greater flux-averaged sediment concentration C, the resulting deposits have greater argillaceous thickness. Figure 39 shows that there is positive correlation between the kaolin composition of the input slurry and the argillaceous thickness of the resulting deposits. The correlations to these concentration properties do not based on correlations with A_c or H^* alone, but only with their product.

$$A_c H^* = A_c \times H^* \tag{15}$$

The kaolin concentration in the inflow slurry is deterministic of the argillaceous content in the deposit. It is useful to inquire how K_c is related to A_c in the deposits. The plot in Figure 40 is of A_c plotted against K_c; we can see a weak trend such that increased kaolin in the deposit is also sign of increased argillaceous content. When considering the results in Figure 39 and the results in Figure 40, it may be inferred that flows with greater concentrations of kaolin have the grains considered to argillaceous based on their size deposit out even if they are in fact silica. We suggest that the deposit becomes more argillaceous simply because the flows have such large sediment concentrations that the finer grains get forced out of suspension. There is work that suggests the same effect of fine sediment coming out of suspension onto bed deposits that occurs in open channel settings such as the Yellow River of China (Ma, 2016).

It is important to state that the numerical results of the trends found in correlating the flow properties to the deposit properties should not be taken as definite. The expressions relating the relevant terms are more numerical guidelines to show overall trends in the results. The results as shown above have both a known and an unknown range of uncertainty. The uncertainty is due to the range of accuracy and precision in measurement instruments, and also to the standard and human error in collecting results. It may be futile to begin to quantify the amount of uncertainty in the results, because some of the error is not defined and also may result in a range of uncertainty that is unacceptable. However, experiments such as these seem to have "unreasonable effectiveness" in determining stratigraphic and geomorphic processes, and as such can be very useful (Paola, 2009).

Future work could be conducted to further explore the nature of HEBs. We suggest a continuation of the present experiments with similar concentration ranges, but with variable slurry inflow rates. Inflow rates greater than those used to date would increase the flow Reynolds number to the range that is considered turbulent flow and turbulence enhanced transitional flow. Alternatively inflow rates reduced from the present work would decrease the flow Reynolds number to a range closer to quasi-laminar plug flow (Baas et al. 2009). We believe the more turbulent range and more laminar range of flows should be explored more because they are not extensively studied in the present work and may result in more deposits of interest, particularly HEBs. The experiments, analysis, and results will be used in numerical models for determining possible HEB locations, structures, etc.

There is a type of transitional flow known as co-genetic sediment density flows that may should be explored. Co-genetic flows are interpreted to produce linked turbidite-debrite type HEB deposits (Sohn, 2000; Amy, 2009; Haughton, 2009). Experiments may include runs that begin with some input slurry sediment concentration of kaolin and silica and at some instance adding large volumes of either silica or kaolin during the flow. The result may form deposits with signatures of linked turbidite-debrite and may represent multiple slump or sidewall failures that may occur in nature during the flow events.

Instead of changing input parameters for each run, future runs may involve setting the same parameters for multiple runs while allowing the bed to evolve. We hypothesize that this may result in a general sequence of deposits corresponding to turbidites overlain by those of HEBs, and then those of debrites as the evolving bed interacts with the density underflows. This sequence is described in many field examples including regions of the Wilcox formation and is interpreted to be due to progradation of the deposits.

The experiments and analysis conducted here were focused on the flow properties of transitional regime density currents and the resulting argillaceous type HEB deposits. The slope and slope break in the current project do not allow for the flow to transform in a way to emplace measurable linked-deposits. For the experiments a surrogate for linked-debrite or linked-turbidite may be present, but not with enough depositional thicknesses to allow characterization. Research on co-genetic flows may also include further exploration of more rapidly changing flow regimes. We suggest further deceleration by way of slope break, the presence of a downstream confinement so as to produce a flow backup, or the transformation from a confined channel to an unconfined basin; all of which may cause downstream changes in the flow Reynolds number in such a way as to produce linked-deposits (Haughton, 2009).

7 Figures for Section Discussion and Direction

This section includes only the figures that are referenced in Section 6 'Discussion and Direction'. Other figures may be found in separate sections following the sections in which they are referenced.

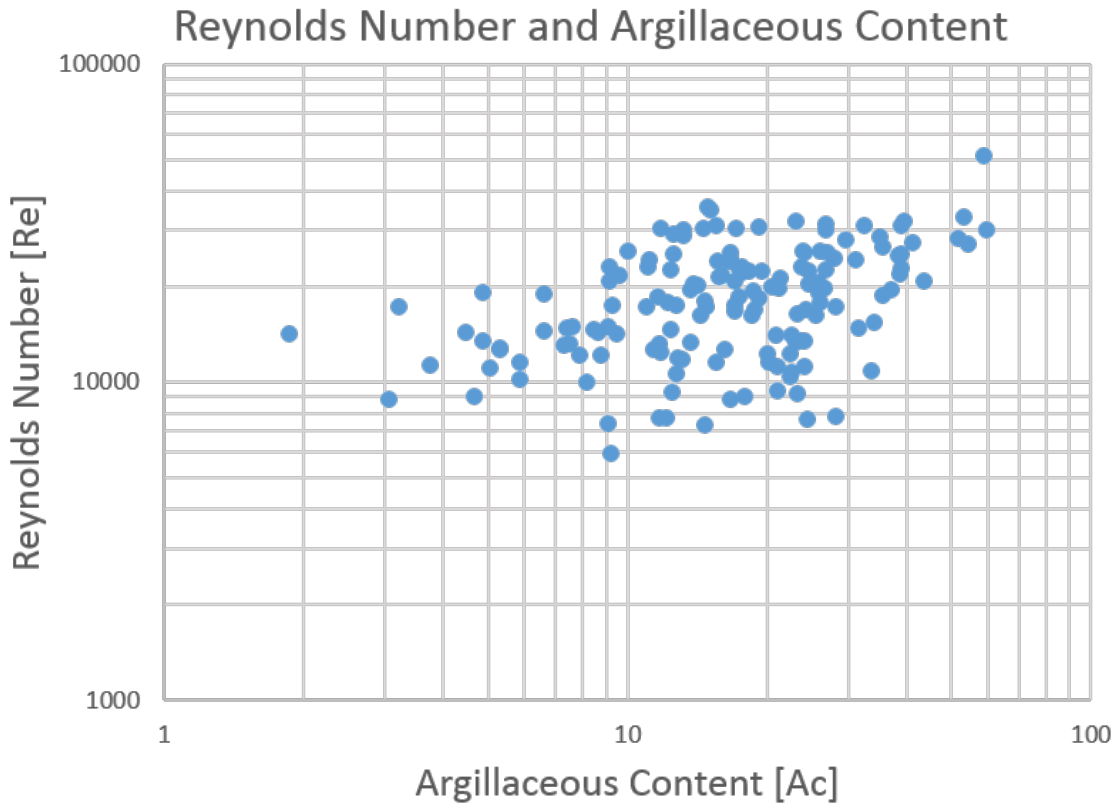

Figure 36: Plot of the data for all runs and locations with Reynolds number R_e and the corresponding argillaceous content A_c. Only a weak correlation may exist, but the deposits with the greatest argillaceous content occur with flows with the greatest Reynolds numbers in the experiments.

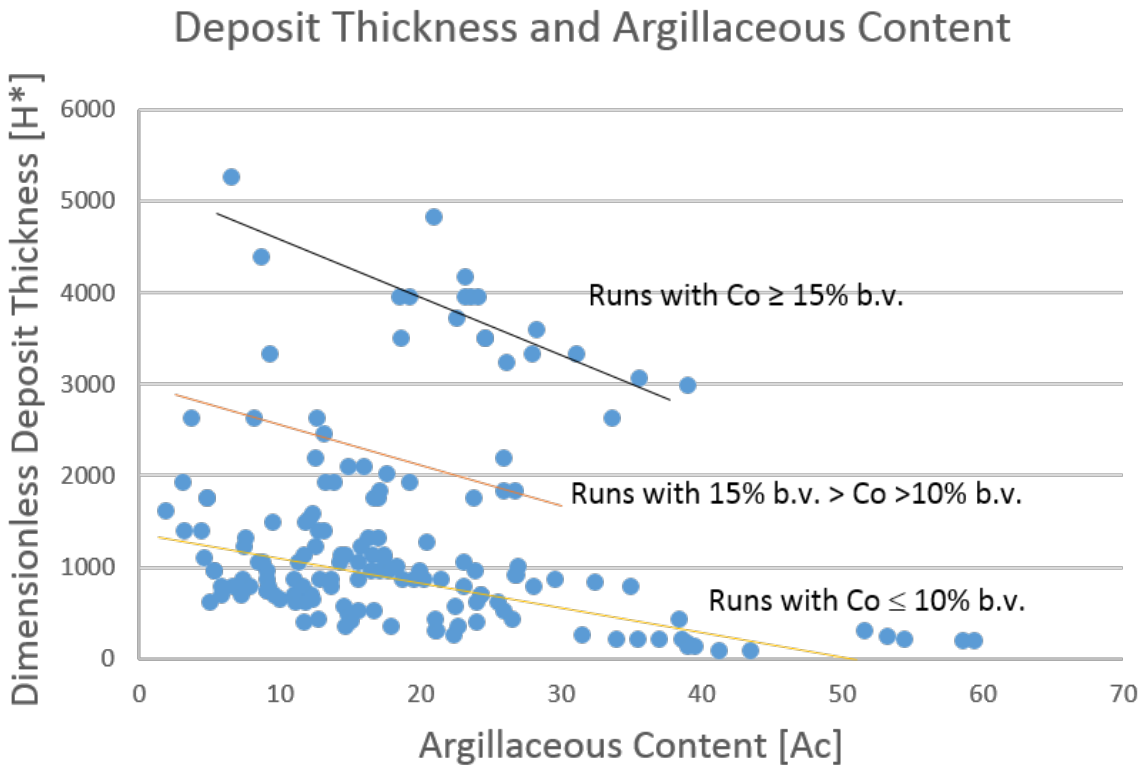

Figure 37: Plot of the data for all runs and locations of dimensionless thickness of deposits H^* and their corresponding argillaceous content. Lines show the trend for data resulting from runs where inflow slurry concentrations were less than or equal to 10% b.v., between 10% b.v. and 15% b.v., and greater than or equal to 15% b.v. from bottom to top respectively

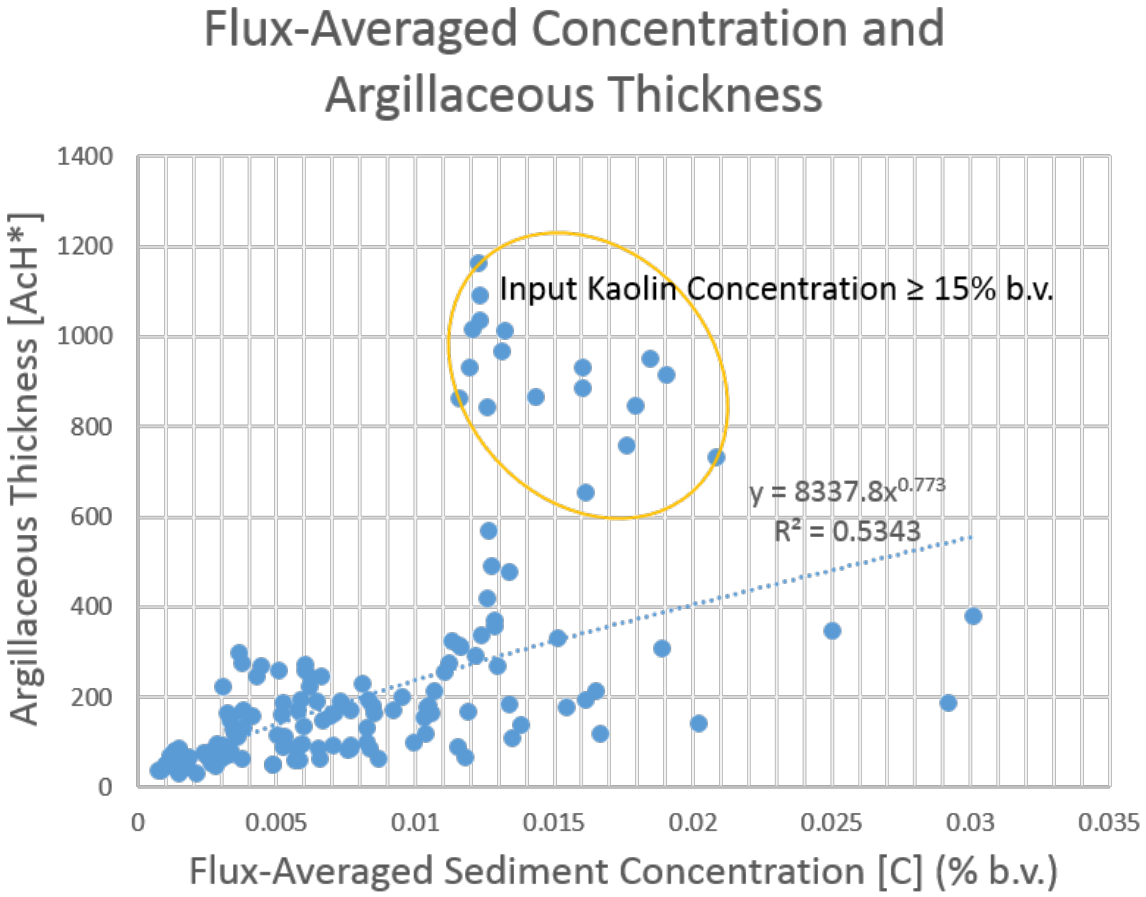

Figure 38: Plot of the data for all runs and locations of flux-averaged sediment concentration C in the flow locations and the corresponding argillaceous thickness $A_c H^*$ of the deposits. Line shows the overall trend in the data. Data points from runs where the kaolin concentration of the inflow slurry was greater than or equal to 15% b.v. are all encircled.

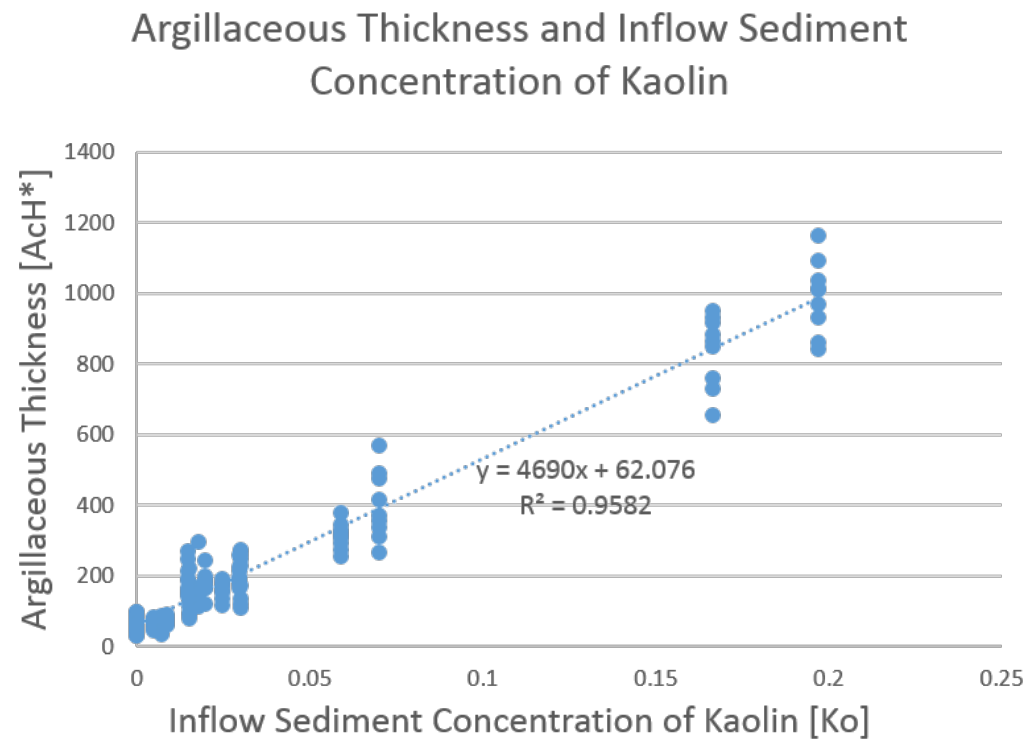

Figure 39: Plot of the data for all runs and locations of sediment concentration of kaolin in the inflow slurry K_o and the corresponding argillaceous thickness A_cH^* of the deposits. Linear trend line shows the positive correlation.

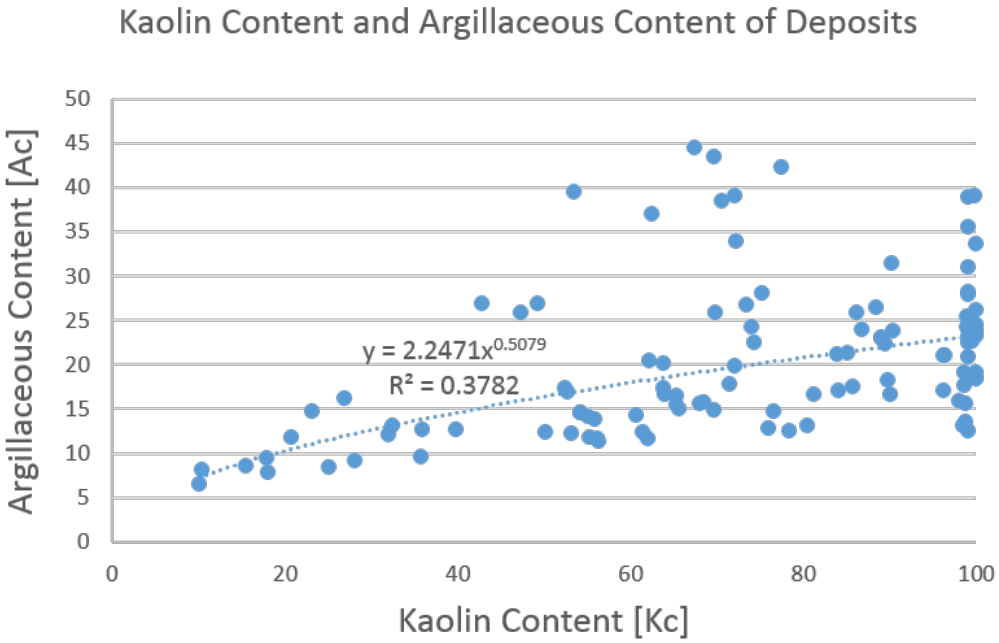

Figure 40: Plot for all locations for runs with non-zero kaolin inflow with data of argillaceous content A_c and kaolin content K_c of the deposits. Power-law trend line shows the very weak correlation.

8 References

Agirrezabala, L. M. and Garcia-Mondejar J. (1994). A coarse grained turbidite system with morphotectonic control (Middle Albian, Ondarroa, Northern Iberia). Sedimentology, 41, 383-407. doi: 10.1111/j.1365-3091.1994.tb02002.x

Amy, L.A., Peachey, S.A., Gardiner, A. A., and Talling, P. J. (2004). Prediction of hydrocarbon recovery from turbidite sandstones with linked-debrite facies: Numerical flow-simulation studies. Marine and Petroleum Geol., 26, 2032-2043. doi: 10.1016/j.marpetgeo.2009. 02.017

Baas, J. H., Best, J. L., Peakall, J., and Wang, M. (2009). A phase diagram for turbulent, transitional, and laminar clay suspension flows. Sedimentology, 79, 162-183. doi: 10.2110/jsr.2009.025

Baas, J. H., Best, J. L. and Peakall, J. (2011). Depositional processes, bedform development and hybrid bed formation in rapidly decelerated cohesive (mud-sand) sediment flows. Sedimentology, 58, 1953-1987. doi: 10.1111/j.1365-3091.2011.01247.x

Cantelli A., Pirmez, C., Johnson, S., and Parker, G. (2011). Morphodynamic and stratigraphic evolution of self-channelized subaqueous fans emplaced by turbidity currents: J. Sed. Research., 81, 233-247. doi: 10.2110/jsr.2011.20

Cantero, M. I., Cantelli, A., Pirmez, C., Balachandar, S., Mohrig, D., Hickson, T.A., Yeh, T-H, Naruse, H. and Parker. G. (2011). Emplacement of massive turbidites linked to extinction of turbulence in turbidity currents. Nature Geoscience, 5, 42-45. doi: 10.1038/ngeo1320

Davis, C., Haughton, P., McCaffrey, W., Scott, E., Hogg, N., and Kitching, D. (2009). Character and distribution of hybrid sediment gravity flow deposits from the outer Fourties Fan, Palaeocene Central North sea, UKCS. Marine Petroleum Geol., 26, 1919-1939. doi: 10.1016/j.marpetgeo.2009.02.015

DeBlasio, F.V., Engvik, L., Harbitz, C.B., and Elverhøi, A. (2004). Hydroplaning and submarine debris flows: J. Geophys. Research, 109, CO1002, doi: 10.1029/ 2002JC001714

Fedele J., Hoyal, D., Barnaal, Z., and Awalt, S. (2014). Experimental on bedforms created by gravity flows. Geophy. Research. Abstracts. EGU General Assembly 2014. id:4514

Fernandez, R.L., Cantelli, A., Pirmez, C., Sequeiros, O. and Parker, G. (2014). Growth Patterns of Subaqueous Depositional Channel Lobe Systems Developed Over A Basement With A Downdip Break In Slope: Laboratory Experiments. J. Sed. Research, 84(3), 168-182. doi: 10.2110/jsr.2014.10

Georgiopoulou, A., Wynn, R.B., Masson, D.G., and Frenz, M. (2009). Linked turbidite-debrite resulting from recent Sahara Slide headwall reactivation. Marine Petroleum Geol., 26, 2021-2031. doi: 10.1016/j.marpetgeo.2009.02.013

Haflidason, H., Lien, R., Sjerup, H.P., Forsberg, C.F., and Bryn, P. (2005).The dating and morphometry of the Storegga Slide: Marine and Petroleum Geol., 22, 123-136, doi: 10.1016/j.marpetgeo.2004.10.008

Haughton, P.D.W., Barker, S.P. and McCaffrey, W.D. (2003) 'Linked' debrites in sand-rich turbidite systems - origin and significance. Sedimentology, 50, 459-482. doi: 10.1046/j.1365-3091.2003.00560.x

Haughton, P.D.W., Davis, C., McCaffrey, W.D., and Barker, S.P. (2009). Hybrid sediment gravity flow deposits - Classification, origin, and significance. Marine and Petroleum Geol., 26, 1900-1918. doi: 10.1016/j.marpetgeo.2009.02.012

Hodgson, D.M. (2009). Distribution and origin of hybrid beds in sand-rich submarine fans of the Tanqua depocentre. Karoo Basin, South Africa. Marine Petroleum Geol., 26, 1940-1956. doi: 10.1016/j.marpetgeo.2009.02.011

Kane, I.A. and Pontén, A.S.M. (2012). Submarine transitional flow deposits in the Paleogene Gulf of Mexico. Geology, 40, 12, 1119-1122. doi: 10.1130/G33410.1

Kineke, G.C., Sternberg, R.W., Trowbridge, J.H. and Geyer, W. R. (1996). Fluid-mud processes on the Amazon continental shelf. Continental Shelf Research, 16 (5-6), 667-696. doi: 10.1016/0278-4343(95)00050-X

Kneller, B. and Buckee C. (2000). The structure and fluid mechanics of turbidity currents: a review of some recent studies and their geological implications. Sedimentology. 47, 62-94. doi: 10.1046/j.1365-3091.2000.047s1062.x

Kostic, S. and Parker, G. (2006). The response of turbidity currents to a canyon-fan transition: internal hydraulic jumps and depositional signatures. J. Hydra. Research, 44, 5 631-653. doi: 10.1201/b16998-96

Kostic, S. and Parker, G. (2007). Conditions under which a supercritical turbidity current traverses an abrupt transition to vanishing bed slope without a hydraulic jump. J. Fluid Mech. 586, 119-145. doi: 10.1017/S0022112007006738

Lastras, G., DeBlasio, F.V., Canals, M., and Elverhøi, A. (2005). Conceptual and numerical modelling of the BIG'95 debris flow, western Mediterranean Sea. J. Sed. Research, 75, 784-797. doi: 10.2110/jsr.2005.063

Lee, S.H., Jung, W., Bahk, J.J., Gardner, J.M., Kim, J.K., and Lee, S.H. (2013). Depositional features of co-genetic turbidite-debrite beds and possible mechanisms for their formation in distal lobated bodies beyond the base-of-slope, Ulleung Basin, East Sea (Japan Sea). Marine Geology, 346, 124-140. doi:10.1016/j.margeo.2013.09.001

Lowe, D.R. and Guy, M. (2000) Slurry-flow deposits in the Britannia Formation (Lower Cretaceous), North Sea: A new perspective on the turbidity current and debris flow problem. Sedimentology, 47, 31-70. doi: 10.1046/j.1365-3091.2000.00276.x

Ma, H., Nittrouer, J., Naito, K., Moodie, A.J., Parker, G. (2016). The exceptional sediment load of a fine-grain meandering river and relation to bedform geometry: an appealing example from the Lower Yellow River, China. Geological Society of America Abstracts with Programs, 48, 7. doi: 10.1130/abs/2016AM-279624

Marr, J. G., Harff, P. A., Shanmugam, G. Parker J. (2001). Experiments on subaqueous sandy gravity flows: The role of clay and water content in flow dynamics, Geo. Soc. Am. Bulletin. 113, 11, 1377. doi: 10.1130/0016-7606(2001)113

Masson, D.G., Wynn, R.B., and Talling, P.J. (2010). Large landslides on passive continental margins: Processes, hypotheses and outstanding questions, in Mosher, D.C., et al., eds., Submarine mass movements and their consequences: 4th International Symposium: Advances in Natural and Technological Hazards Research. 153-166. doi: 10.1007/978-90-481-3071-9

Migeon, S., Savoye, B., Babonneau. N., and Spy-Anderson F. (2004). Processes of sediment-wave construction along the present Zaire deep-sea meandering channel; role of meanders and flow stripping. J. Sed. Research, 74(4), 580-598. doi: 10.1306/091603740580

Mohrig, D., Ellis, C., Parker, G., Whipple, K. X., and Hondzo, M. (1998). Hydroplaning of subaqueous debris flows. Geol. Soc. Am. Bulletin, 110(3), 387-394. doi: 10.1130/0016-7606(1998)110

Mohrig, D., Elverhoi, A. and Parker, G. (1999). Experiments on the relative mobility of muddy subaqueous and subaerial debris flows, and their capacity to remobilize antecedent deposits. Marine Geol., 154, 117-129. doi: 10.1016/S0025-3227(98)00107-8

Pedocchi, F. and Garcia, M. H. (2006). Evaluation of the LISST-ST instrument for suspended particle size distribution and settling velocity measurements. Continental Shelf Research, 26(8), 943-958. doi: 10.1016/j.csr.2006.03.006

Pedocchi, F. and Garcia, M. H. (2007). Observations in a large oscillatory water-sediment tunnel. Hydra. Measurements & Experimental Methods, conference publication.

Piper, D.J.W., and Normark. W.R. (2009). The processes that initiate turbidity currents and their influence on turbidites: a marine geology perspective. J. Sed. Research, 79, 347-362. doi: 10.2110/jsr.2009.046

Pirmez, C. and Imran, J. (2003). Reconstruction of turbidity currents in Amazon Channel. Marine Petroleum Geol., 20, 823-849. doi: 10.1016/j.marpetgeo.2003.03.005

Postma, G., Nemec, W., and Kleinspehn, L. (1988). Large floating clasts in turbidites: a mechanism for their emplacement. Sed. Geol., 58, 47-61. doi: 10.1016/0037-0738(88)90005-X

Pyles, D.R. and Jennette, D.C. (2009). Geometry and architectural associations of cogenetic debrite-turbidite beds in basin-margin strata, Carboniferous Ross Sandstone (Ireland): Applications to reservoir located on the margins of structurally confined submarine fans. Marine Petroleum Geol., 26, 1974-1996. doi: 10.1016/j.marpetgeo.2009.02.018

Sequeiros, O. E., Naruse H., Endo, N., Garcia, M. H., and Parker G. (2009). Experimental study on self-accelerating turbidity currents, J. Geophys. Research, 114, C05025. doi: 10.1029/2008JC005149

Sequeiros, O.E., Spinewine, B., Garcia, M.H., Beaubouef, R.T., Sun, T., and Parker, G. (2009). Experiments on wedge-shaped deep sea sedimentary deposits in minibasins and/or on channel levees emplaced by turbidity currents. Part I. Documentation of the flow. Sed. Research. 79, 593-607. doi: 10.2110/jsr.2009.064

Sequeiros, O. E., Spinewine, B., Beaubouef, R. T., Sun, T., Garcia, M. H. and Parker, G. (2010). Bedload transport and bed resistance associated with density and turbidity currents. Sedimentology, 57, 1463-1490. doi: 10.1111/j.1365-3091.2010.01152.x

Sohn, Y.K. (2000). Depositional processes of submarine debris flows in the Miocene fan deltas, Pohang Basin, SE Korea with special reference to flow transformation. Sed. Research. 70, 491-503. doi: 10.1306/2DC40922-0E47-11D7-8643000102C1865D

Spinewine, B., Sequeiros, O.E., Garcia, M.H., Beaubouef, R.T., Sun, T., Savoye, B., and Parker, G. (2009). Experiments on wedge-shaped deep sea sedimentary deposits in minibasins and/or on channel levees emplaced by turbidity currents. Part II. Morphodynamic evolution of the wedge and of the associated bedforms. J. Sed. Research. 79, 608-628. doi: 10.2110/jsr.2009.065

Stevenson, C.J., Talling, P.J., Masson, D.G., Sumner, E.J., Frenz, M., and Wynn, R.B. (2014). The spatial and temporal distribution of grain-size breaks in turbidites. Sedimentology. 61, 1120-1156. doi: 10.1111/sed.12091

Sumner, E.J., Talling, P.J., and Amy, L.A. (2009).The deposits of flows transitional between turbidity currents and debris flow. Geology, 37, 991-994, doi:10.1130/G30059A.1

Sumner, E.J., Talling, P.J., Amy, L.A., Wynn, R.B., Stevenson, C., and Frenz, M. (2012). Facies architecture of individual basin-plain turbidites: Comparison with existing models and implications for flow processes. Sedimentology, 59, 1850-1857, doi:10.1111/j.1365-3091.2012.01329.x

Sylvester, Z. and Lowe, D.R. (2004). Textural trends in turbidites and slurry beds from the Oligocene flysch of the East Carpathians, Romania. Sedimentology, 51, 945-972. doi: 10.1111/j.1365-3091.2004.00653.x

Talling, P.J., Amy, L.A., Wynn, R.B., Peakall, J., and Robinson, M. (2004). Beds comprising debrite sandwiched within co-genetic turbidite: Origin and widespread occurrence in distal depositional environments. Sedimentology, 51, 163-194. 10.1111/j.1365-3091.2004.00617.x

Talling, P.J., Wynn, R.B., Masson, D.G., Frenz, M., Cronin, B.T., Schiebel, R., Akhmetzhanov, A.M., Dallmeier-Tiessen, S., Benetti, S., Weaver, P.P.E., Georgiopoulou, A., Zühlsdorff, C., and Amy, L.A. (2007). Onset of submarine debris flow deposition far from original giant landslide. Nature, 450, 541-544. doi: 10.1038/nature06313

Talling, P.J. (2013). Hybrid submarine flows comprising turbidity current and cohesive debris flow: deposits, theoretical and experimental analyses, and generalized models. Geosphere. 9, 3, 460-488. doi:10.1130/GES00793.1

Toniolo, H., Harff, P., Marr, J. and Parker, G. (2004). Experiments on reworking by successive unconfined subaqueous and subaerial muddy debris flows. J. Hydra. Eng., 130(1), 38-48. doi: 10.1061/(ASCE)0733-9429(1994)120:1(104)

Winn, R. D., Jr. and Dott, R. H. (1977). Large-scale traction-produced in deep-water channel-fan conglomerates in southern Chile. Geology, 5, 41-44. doi: 10.1130/0091-7613(1977)5¡41:LTSIDF¿2.0.CO;2

Xu, J.P., Noble, M.A., and Rosenfeld, L.K. (2004). In-situ measurements of velocity structure within turbidity currents. Geophys. Research Letters, 31, L09311. doi: 10.1029/ 2004GL019718

Yu, B. Cantelli, A. Marr, J. G., Pirmez C., O'Byrne C., and Parker, G. (2006). Experiments on self-channelized subaqueous fans emplaced by turbidity currents and dilute mudflows. J. Sed. Research. 76, 889-902. Doi:10.2110/jsr.2006.069

Appendix A

```
function [x,t,DopplerVel,AmplData] = uvp_reader(filename)
% reads UVP files
% DopplerVel: Velocity in mm/s
% AmplData: Dimensionless Echo Amplitude sampled into a 14 Bits +/-2.5V AD
% converter (8'191=2.5V; -8'192=-2.5V)
% x: distance from the sensor in m
% t: time in seconds
% SampleTime: Sampling time in mili seconds
% CycleDelay: Tyme delay between cycles
% nChannels: number of channels in a profile
% nProf: number of profiles
% Blocks: Number of blocks=number of sensors * NumberOfCycles
% VelRange: Absolute value of the velocity range
% MinVel: Minimum velocity
% MaxVel: Maximum velocity
% Note: if the values reported in the DopplerVel vector are outside the
% {MinVel MaxVel} interval these values should be discarded.
% Gain Start: Gain factor at the sensor (see pg 3.14 of the uvp manual)
% GainEnd: Gain factor at MaxDepth
%% ---------------START---------------
fid = fopen(filename);
%File Header:
fread(fid,64,'char');
fread(fid,1,'int64');
% Number of profiles
nProf = fread(fid,1,'int32');
fread(fid,1,'int32');
% Record amplitud
flags = fread(fid,1,'int32');
fread(fid,1,'int32');
% Number of channels
nChannels = fread(fid,1,'int32');

fread(fid,1,'int32');
fread(fid,1,'int64');
%% ---------------PROFILES---------------
DopplerData = zeros(nChannels,nProf);
AmplData = zeros(nChannels,nProf);
profileTime = zeros(1,nProf);
for j=1:nProf
    fread(fid,1,'int32');
    fread(fid,1,'int32');

    profileTime(j) = fread(fid,1,'int64');

    DopplerData(1:nChannels,j) = fread(fid,nChannels,'int16');

    if flags == 1
        AmplData(1:nChannels,j)=fread(fid,nChannels,'int16');
```

```
    end
end

fgetl(fid);
%% ---------------PREPROCESSING---------------
% frequency of the sensor used:
Frequency = fscanf(fid,'Frequency=%i \n');
% distance from the sensor to the first channel recorded in mm
StartChannel = fscanf(fid,'StartChannel=%g \n');
% distance between channels in mm
ChannelDistance = fscanf(fid,'ChannelDistance=%g \n');
% chanel width in mm, if overlap =0% is equal to channel distance
fscanf(fid,'Width=%g \n');
% Maximum distance from the sensor that will be recorded in mm
MaxDepth = fscanf(fid,'MaximumDepth=%g \n');
% Sound speed in m/s:
SoundSpeed = fscanf(fid,'SoundSpeed=%i \n');
% Angle in deg if using one sensor
Angle = fscanf(fid,'Angle=%g \n');
% Gain factor at the sensor (see pg 3.14 of the uvp manual)
fscanf(fid,'GainStart=%i \n');
% Gain factor at MaxDepth
fscanf(fid,'End=%i \n');
% US voltage aplied to the transducer in V
fscanf(fid,'Voltage=%i \n');
% Repetitions (default=32 )
fscanf(fid,'Iterations=%i \n');
% Noise level filter (default=4)
fscanf(fid,'NoiseLevel=%i \n');
% Number of wave lengths in and emited pulse (See pg 5.37 of the uvp manual)
fscanf(fid,'CyclesPerPulse=%i \n');
% same as nChannels
fscanf(fid,'TriggerMode=%i \n');
fscanf(fid,'Name=%s \n');
fscanf(fid,'ProfileLength=%i \n');
% number of profiles per block
fscanf(fid,'sPerBlock=%i \n');
% Number of blocks=number of sensors * NumberOfCycles
fscanf(fid,'Blocks=%i \n');
% same as flags
fscanf(fid,'AmplitudeStored=%i \n');
% same as flags
fscanf(fid,'DoNotStoreDoppler=%i \n');
% Minimum possible value of raw data
fscanf(fid,'RawDataMin=%i \n');
% Maximum possible value of raw data
fscanf(fid,'ax=%i \n');
% RawDataMax-RawDataMin
RawDataRange = fscanf(fid,'RawDataRange=%i \n');
% Minimum possible value of amplitude data
fscanf(fid,'AmplDataMin=%i \n');
```

```
% Maximum possible value of amplitude data
fscanf(fid,'ax=%i \n');
% -1=Negative range, 0=symetric range, 1=positive range
fscanf(fid,'VelocityInterpretingMode=%i \n');
% 0= Minimum sampling time, 1=user defined
fscanf(fid,'UserSampleTime=%i \n');
% Sample time inside a block
fscanf(fid,'SampleTime=%i \n');
% 1=use multiplexer, 0=do not use multiplexer
fscanf(fid,'UseMultiplexer=%i \n');
% 1=flowmaping option on, 0=off
fscanf(fid,'FlowMapping=%i \n');
% First channel recorded
fscanf(fid,'irstValidChannel=%i \n');
% Last channel recorded
fscanf(fid,'LastValidChannel=%i \n');
% 0=Paralel, 1=Circular (see pg 5.30)
fscanf(fid,'FlowRateType=%i \n');
% See pg 5.25
fscanf(fid,'PeriodEnhOffset=%i \n');
% See pg 5.25
fscanf(fid,'Period=%i \n');
% See pg 5.25
fscanf(fid,'EnhNCycles=%i \n');
%Multiplexer Parameters
fgetl(fid);
fgetl(fid);
fgetl(fid);
% Number of cycles
fscanf(fid,'NumberOfCycles=%i \n');
% delay between cycles
fscanf(fid,'CycleDelay=%i \n');

fscanf(fid,'Version=%i \n');
fclose(fid);
%% ---------------PROCESSING---------------
% See pg 3.9 of the uvp manual
VelRange = (SoundSpeed^2)/(4*Frequency*MaxDepth/1000);
% Velocity in mm/s
DopplerVel = DopplerData.*VelRange.*1000./(RawDataRange*sin(Angle*pi/180));
% x: distance from the sensor in m
x = ((0:nChannels-1).*ChannelDistance + StartChannel)';
% t: time in seconds
t = profileTime.*1e-7;
% loads file under specified name and runs functions
filename = 'run0001.mfprof';
[x,t,DopplerVel,AmplData] = uvp_reader(filename);
% end of code
```

Appendix B

All of the data from measurements are given below. The 'Run ID' column lists the name given to each experimental run; these are used to organize the runs. The column 'UVPfile' indicates the name given to each measurement file from the UVP during each run. The 'Location' column identifies where along the flume the corresponding measurements were taken. The 'H(cm)' column gives the thickness of the resulting deposit from that run in centimeters. The 'L(cm)' column gives the location of the measurements as a distance from the inlet diffuser at the upstream end. The 'Kc%' column gives the found percent of the total grains that is kaolin grains as specified in Eq. 12. The 'Ac%' columns give the relative percentage of fine grains as specified in Eq. 11 found within the corresponding deposit. The 'U (m/s)' column are the results of the layer-averaged velocity for each location in meters per second. The 'C(m^3/m^3)' column are the results of the flux-averaged volumetric concentration found for the flow at each location. The '$C_o(m^3/m^3)$' column are the volumetric concentration of the inflow for each run. Lastly, the 'Re#' and 'Fr#' column respectively are the resulting Reynolds number and densimetric Froude number for the density currents as computed from Eq. 1 and Eq. 6, respectively.

Table 3: Measurement data from all of the experimental runs.

Run ID	UVPfile	Location	H (cm)	L (cm)	Kaolin %	AC%	U (m/s)	C (m3/m3)	Co (m3/m3)	Re #	Fr #
Explore1	n/a	alpha	6.00	152		0.3747	0.080000	0.030000	0.180176	5366.71401	0.36482
Explore1	n/a	alpha-beta	4.50	198			0.075000	0.020000	0.180176	9051.11236	0.34035
Explore1	n/a	beta	3.30	320		1.1736	0.070000	0.010000	0.180176	11790.45931	0.41010
Explore2	upstream	alpha-beta up	4.00	196		0.2915	0.197756	0.040000	0.130413	8879.12672	0.86907
Explore2	downstream	alpha-beta down	3.00	203		0.3363	0.142524	0.020000	0.130413	15118.74545	0.68985
Show1	run0002	beta-75	3.00	292			0.155037		0.020623	44957.83231	1.00453
Show1	run0003	alpha-beta	4.00	198			0.064703		0.020623	9981.30276	0.57694
Show1	run0004	alpha-beta	4.00	198			0.062910		0.020623	9704.59258	0.56095
Show1	run0005	beta-160	2.00	381		0.2101	0.057814	0.005000	0.020623	16637.44480	0.37602
Show1	run0006	beta-50	2.50	267			0.077861		0.020623	11449.07293	0.70844
Show1	run0007	beta-50	2.50	267			0.089663		0.020623	9868.13232	0.94300
Show1	run0008	beta-50	2.50	267			0.104301		0.020623	11479.20747	1.09695
Show2	run0009	alpha-beta up	2.30	196		0.4691	0.035726	0.008000	0.024452	7726.33884	0.20980
Show2	run0010	alpha-beta down	2.00	203		0.5616		0.008000	0.024452	7889.26825	0.01343
Show2	run0011	alpha-beta down	2.00	203					0.024452	13505.88480	0.36537
Show2	run0012	beta center	1.50	320		0.6123	0.070933	0.008000	0.024452	15340.38724	0.41500
Show2	run0013	beta center	1.50	320		0.6123	0.071438	0.008000	0.024452	15449.64375	0.41795
Show2	run0014	up beta-gamma-80	1.20	356		0.9649	0.093947	0.008000	0.024452	20317.61995	0.54965
Show2	run0015	up beta-gamma-10	1.40	427		1.2101	0.029571	0.008000	0.024452	20392.98825	0.55169
Show2	run0016	gamma-40	1.00	488		1.0521	0.041737	0.008000	0.024452	17100.72866	0.63262
Show2	run0017	center gamma	1.00	564		1.5354	0.010322	0.008000	0.024452	2165.23064	0.06132
Pulse1	run_0002	alpha130	2.00	152		16.9043	0.079430	0.001000	0.059250	8958.02784	1.86581
Pulse1	run_0004	beta170	1.50	330		19.7307	0.091792	0.000607	0.059250	13450.08194	2.42774
Pulse1	run_0006	gamma40	1.10	483		22.8192	0.098592	0.000607	0.059250	15891.18291	2.48625
Pulse1	run_0008	gamma170	0.70	572		27.2042	0.067053	0.000607	0.059250	10611.20136	1.70650
Pulse1	run_0011	delta220	1.31	838		36.6730	0.014489	0.000607	0.059250	3948.86248	0.27993
Pulse2	run_0001	beta140	0.75	330		11.0445	0.021149	0.001992	0.018156	3368.15547	0.29586
Pulse2	run_0002	gamma70	0.56	508		49.1901	0.036149	0.001292	0.018156	5821.06407	0.62508
Pulse2	run_0003	gamma70	0.56	508		49.1901	0.033760	0.000892	0.018156	5983.93898	0.66988
Pulse2	run_0004	gamma150	0.50	559		57.6742	0.023454	0.000692	0.018156	2268.05004	0.71545
Pulse2	run_0006	gamma190	0.50	584		51.6017	0.015958	0.000592	0.018156	3905.09257	0.32965
Pulse2	run_0007	delta70	0.50	737		49.1869	0.045983	0.000572	0.018156	7344.32938	1.19609
Pulse2	run_0008	delta150	0.44	813		52.8447	0.007318	0.000552	0.018156	1233.24091	0.18866
Pulse2	run_0009	eps210	0.25	1092		61.2102	0.023364	0.000532	0.018156	1780.26697	0.91237

Table 3: (cont.).

Run ID	UVPfile	Location	H (cm)	L (cm)	Kaolin %	AC%	U (m/s)	C (m3/m3)	Co (m3/m3)	Re #	Fr #
Pulse3	run0004	gam170	1.3125	584.2		50.63693631	0.075373213	0.0024525	0.04113571	11213.50269	0.978626889
Pulse3	run0005	del50	1.25	711.2		41.00998482	0.054852918	0.002600077	0.04113571	11433.74897	0.584175492
Pulse3	run0006	del190	1.25	863.6		41.84036807	0.096664486	0.0030186	0.04113571	18141.05232	1.0059445
Pulse3	run0007	eps80	1.1875	990.6		44.54140828	0.079669249	0.0028944	0.04113571	16004.37712	0.818609196
Pulse4	run0008	gamma 180	1.6875	571.5	88.40884015	39.07809219	0.069219584	0.01129772	0.072098602	14698.50547	0.336441643
Pulse4	run0010	delta 140	1.25	825.5	93.36292551	31.67316732	0.068036416	0.008603507	0.072098602	15874.13752	0.367496944
Pulse4	run0011	eps-zet	1.2	1168.4	99.548936	31.98959688	0.073597841	0.010586941	0.072098602	18767.12029	0.33877052
Pulse5	run0001	alpha 125	3	152.4	89.44630105	22.81751299	0.07459996	0.067355968	0.101212248	1057.321647	0.354079591
Pulse5	run0002	beta 70	2.2	279.4	59.15312428	30.84260945	0.071977796	0.013366002	0.101212248	4136.426929	0.61178778
Pulse5	run0004	beta 170	1.4	355.6	57.59150079	35.59214468	0.068797533	0.00829263	0.101212248	4697.771449	0.703490172
Pulse5	run0005	gamma 70	1.3	508	48.40921255	45.42400131	0.047272886	0.0033366	0.101212248	5492.755864	0.594182349
Show3	run0001	beta 210	0.6875	381	57.37479927	26.35360089	0.060272002	0.003649403	0.024553536	10933.9773	0.581673224
Show3	run0003	delta 100	1	762	77.29563426	44.219332	0.044451745	0.0046308	0.024553536	6319.780133	0.473924066
Show3	run0004	beta 210	0.6875	381	57.37479927	26.35360089	0.063183493	0.01378839	0.024553536	9605.33098	0.324252451
*Main1	run0001	b-g	2	441.96	60.8726336	20.59617885	0.080587616	0.00843841	0.030360385	7639.370781	0.693446404
Main1	run0002	g	2	563.88	77.5921258	25.85741426	0.054423491	0.007435456	0.030360385	6134.065325	0.459956718
Main1	run0003	g-d	1.75	680.72	98.85939566	25.80741926	0.056639535	0.007814423	0.030360385	6359.06048	0.46693409
Main1	run0004	d	1	805.18	89.118005	33.84661534	0.049317646	0.007849297	0.030360385	8510.056889	0.325941082
Main1	run0005	d-e	0.5	924.56	98.993	34.66493299	0.050314367	0.008339286	0.030360385	8636.714337	0.322611428
Main1	run0006	e-z	0.4	1163.32	83.86771414	35.42354235	0.055279358	0.007687106	0.030360385	9554.877701	0.369176214
Bound1	run0001	b	4.5	320.04	100	23.20332033	0.132440334	0.019058068	0.166554523	9170.643389	0.821100261
Bound1	run0002	b-g	4.5	441.96	100	23.61008302	0.15615643	0.016023601	0.166554523	13518.375	0.968020652
Bound1	run0003	g	4.5	563.88	100	24.05518896	0.134508127	0.018440399	0.166554523	13467.46832	0.708685707
Bound1	run0004	g-d	4.5	680.72	100	18.51185119	0.138214446	0.020857198	0.166554523	16158.69339	0.618399999
Bound1	run0005	d	4.5	805.18	100	19.23807619	0.131582654	0.017592394	0.166554523	18350.94502	0.603376597
Bound1	run0006	d-e	4	924.56	100	24.64507099	0.111807032	0.014327589	0.166554523	20301.29012	0.510831551
Bound1	run0007	e	4	1046.48	100	18.65186519	0.096707161	0.016130795	0.166554523	19380.24782	0.390908816
Bound1	run0009	e-z	3.7	1163.32	100	26.13097411	0.100333193	0.017934001	0.166554523	17820.11073	0.402656135
Bound1	run0011	b-g	3	441.96	100	33.61008302	0.108589848	0.016023601	0.166554523	10899.20297	0.622829083
Main2	run0001	b	1.4	320.04	61.44593838	12.494998	0.086164503	0.010295584	0.049254267	9260.958698	0.623552317
Main2	run0003	b-g	1.1	441.96	72.06858205	19.9759928	0.107761279	0.016129686	0.049254267	12295.58769	0.580023833
Main2	run0004	g	1	563.88	63.7814016	20.24607382	0.104825975	0.015466034	0.049254267	11548.52214	0.587249801
Main2	run0005	g-d	0.9	680.72	88.96890687	23.05461092	0.08437252	0.008451151	0.049254267	13306.46468	0.560307886
Main2	run0006	d	0.8	805.18	98.94300375	24.29485897	0.088020392	0.007692269	0.049254267	16868.4449	0.558061232

Table 3: (cont.).

Run ID	UVPfile	Location	H (cm)	L (cm)	Kaolin %	AC%	U (m/s)	C (m3/m3)	Co (m3/m3)	Re #	Fr #
Main2	run0007	d-e	0.7	924.56	98.88127264	25.53510702	0.086594805	0.006933386	0.049254267	16225.80463	0.587051437
Main2	run0008	e	0.6	1046.48	86.16425253	25.94518904	0.089095046	0.005976495	0.049254267	19154.65447	0.609999949
Main2	run0009	e-z	0.5	1163.32	88.40466941	26.55062025	0.085717951	0.005019604	0.049254267	19818.51358	0.619913581
Main3	run0002	bmid	1.3	320.04	62.05829737	11.69883012	0.067514165	0.008234478	0.030181936	7718.794605	0.536107244
Main3	run0003	b-g	1	441.96	75.94256512	12.80384115	0.069568792	0.005284491	0.030181936	11912.72125	0.571332827
Main3	run0004	gmid	0.9	563.88	75.16664952	28.06842053	0.046499784	0.003049192	0.030181936	7805.129946	0.51147382
Main3	run0005	g-d	0.8	680.72	73.9201308	24.35487097	0.042923055	0.003800524	0.030181936	7615.37586	0.41048142
Main3	run0006	dmid	0.65	805.18	74.28744208	22.49	0.045733818	0.003428963	0.030181936	10416.48848	0.405305884
Main3	run0007	d-e	0.5	924.56	96.18887206	21.04	0.048338214	0.003057401	0.030181936	11244.86182	0.449343568
Main3	run0008	emid	0.45	1046.48	86.70805164	24.04240424	0.045856427	0.002854166	0.030181936	11151.19846	0.431729064
Main3	run0010	e-z	0.4	1163.32	99.4745	22.67453491	0.049428622	0.002650931	0.030181936	14072.70564	0.446471028
Main4	run0001	bmid	0.5	320.04	35.89705592	12.72254451	0.057994977	0.002699819	0.009968268	10606.18123	0.650024163
Main4	run0002	b-g	0.45	441.96	56.20257767	11.69883012	0.05948348	0.002786231	0.009968268	13154.16202	0.5967047
Main4	run0003	gmid	0.4	563.88	76.50809943	14.71	0.031519144	0.001537058	0.009968268	7328.639159	0.414545392
Main4	run0004	g-d	0.4	680.72	71.43398833	17.90816595	0.032596429	0.001556085	0.009968268	9026.918303	0.390413927
Main4	run0005	dmid	0.35	805.18	96.2903026	21.1063319	0.042183794	0.001575111	0.009968268	9432.542774	0.5
Main4	run0006	d-e	0.3	924.56	90.23745257	31.52630526	0.043420017	0.001461998	0.009968268	14728.42372	0.484832256
Main4	run0007	emid	0.25	1046.48	72.26347864	33.96980906	0.041248698	0.001348885	0.009968268	15462.35813	0.456199829
Main4	run0008	e-z	0.25	1163.32	67.36217395	35.486654	0.046297044	0.001336502	0.009968268	18795.7924	0.494294659
Main4	run0009	z	0.25	1290.32	62.46086925	37.00349895	0.054055314	0.001324118	0.009968268	19623.34376	0.613175412
*Bound2	run0001	bmid	3	320.04	0	3.739626037	0.109580387	0.0099623	0.089465671	11360.3211	0.822128499
Bound2	run0002	b-g	2	441.96	0	4.877561219	0.112279981	0.008382802	0.089465671	13435.88484	0.862612149
Bound2	run0003	gmid	1.5	563.88	0	7.58	0.098101195	0.008255679	0.089465671	14936.3237	0.671241318
Bound2	run0004	g-d	1.4	680.72	0	7.512253676	0.080217402	0.007656443	0.089465671	13201.39882	0.549944332
Bound2	run0005	dmid	1.2	805.18	0	8.742622787	0.076215232	0.007057207	0.089465671	12183.09242	0.553871463
Bound2	run0006	d-e	1.1	924.56	0	9.04909509	0.069568839	0.006501341	0.089465671	14872.35969	0.456680882
Bound2	run0007	emid	1	1046.48	0	10.97	0.068111792	0.005945474	0.089465671	17284.57111	0.430195055
Bound2	run0008	e-z	0.9	1163.32	0	11.66883312	0.068260057	0.005842927	0.089465671	18617.96941	0.419675077
Bound2	run0009	z	0.8	1290.32	0	12.2536761	0.066722831	0.005740381	0.089465671	17732.56068	0.419457412
Bound2	run0010	b-g end	2	441.96	0	4.877561219	0.124339515	0.007656443	0.089465671	19051.37355	0.883438704
Main5	run0000	bmid	3	320.04	10.31072551	8.140814081	0.10633671	0.010667162	0.098305799	9950.776131	0.808331065
Main5	run0001	b-g	1.7	441.96	20.67714664	11.81	0.116597637	0.010449099	0.098305799	12389.20843	0.841569344
Main5	run0002	gmid	1.6	563.88	39.80731246	12.76744651	0.1260893	0.010464875	0.098305799	17396.22945	0.795008002
Main5	run0003	g-d	1.8	680.72	53.17206773	12.35123512	0.096305651	0.008326341	0.098305799	14579.31274	0.658101802

Table 3: (cont.).

Run ID	UVPfile	Location	H (cm)	L (cm)	Kaolin %	AC%	U (m/s)	C (m3/m3)	Co (m3/m3)	Re #	Fr #
Main5	run0004	dmid	1.5	805.18	52.7299504	17.02510753	0.093983908	0.006187807	0.098305799	17452.34469	0.67981987
Main5	run0005	d-e	1.45	924.56	62.17778025	20.48614584	0.10320679	0.006038037	0.098305799	19862.21434	0.742839287
Main5	run0006	emid	1.4	1046.48	68.49292774	15.76315263	0.096533572	0.005888267	0.098305799	21539.07948	0.653859704
Main5	run0007	e-z	1.3	1163.32	63.90748725	16.63833617	0.108318076	0.006481184	0.098305799	24432.3565	0.693708299
Main5	run0008	z	1.2	1290.32	68.00882088	15.6	0.10476385	0.007074101	0.098305799	23949.08041	0.63614449
Main6	run0001	bmid	1.75	320.04	31.91685592	12.16121612	0.098558283	0.02918266	0.049112941	7716.407457	0.424291946
Main6	run0002	b-g	1.7	441.96	17.79314944	9.49	0.120515937	0.020195478	0.049112941	14259.14587	0.550415697
Main6	run0003	gmid	1.5	563.88	26.8750045	16.26	0.108164705	0.016514047	0.049112941	12649.77821	0.564479596
Main6	run0004	g-d	1.3	680.72	54.15243265	14.67146715	0.113201748	0.011920076	0.049112941	18081.67575	0.61564864
Main6	run0005	dmid	1.25	805.18	52.37154776	17.39478157	0.111747781	0.007326104	0.049112941	22766.23015	0.705432106
Main6	run0007	d-e	1.2	924.56	55.04889143	14.22426728	0.096635143	0.006677215	0.049112941	20228.34894	0.632362653
Main6	run0008	emid	1.15	1046.48	42.75850304	26.96269627	0.101187202	0.006028326	0.049112941	25552.03037	0.636340869
Main6	run0010	e-z	1.1	1163.32	65.22951184	16.53834617	0.092621956	0.00516728	0.049112941	24027.59493	0.622921394
Main6	run0011	zmid	1.05	1290.32	49.24097452	26.87268727	0.09493749	0.004306234	0.049112941	22554.39874	0.733148084
Bound3	run0001	bmid	2.2	320.04	0	3.060306031	0.081192591	0.005643446	0.049667328	8832.258493	0.807976123
Bound3	run0002	b-g	1.6	441.96	0	4.46	0.108512581	0.006559791	0.049667328	14286.01878	0.906795771
Bound3	run0003	gmid	1.1	563.88	0	5.291058212	0.092190726	0.004882094	0.049667328	12610.84598	0.878939211
Bound3	run0004	g-d	1	680.72	0	7.4	0.088661318	0.003777253	0.049667328	14857.67359	0.87147321
Bound3	run0005	dmid	0.9	805.18	0	6.62	0.104397991	0.002672412	0.049667328	18870.1556	1.178084214
Bound3	run0006	d-e	0.85	924.56	0	9.127261821	0.11077132	0.002520748	0.049667328	22985.32835	1.201632076
Bound3	run0007	emid	0.8	1046.48	0	11.05889411	0.102170318	0.002369084	0.049667328	23028.89507	1.097276786
Bound3	run0008	e-z	0.75	1163.32	0	10.0189981	0.116192257	0.002659509	0.049667328	25770.79683	1.186563869
Bound3	run0009	z	0.7	1290.32	0	11.11222244	0.095425258	0.002949934	0.049667328	24306.61514	0.862825384
Bound3	run0010	d-e	0.85	924.56	0	9.127261821	0.096994433	0.002520748	0.049667328	20879.99133	1.033025232
Bound3	run0011	gmid	1.1	563.88	0	5.291058212	0.084564068	0.004882094	0.049667328	12863.15909	0.764548566
Main7	run0000	bmid	1.2	320.04	25.08778881	8.479152085	0.111688284	0.01153736	0.029454806	14664.74027	0.685292042
Main7	run0001	b-g	0.9	441.96	17.96033303	7.86	0.087549141	0.008687584	0.029454806	12152.26011	0.612730106
Main7	run0002	gmid	0.8	563.88	35.69645072	9.580958096	0.12182974	0.011805626	0.029454806	21554.6175	0.633087658
Main7	run0003	g-d	0.75	680.72	50.07617443	12.37371211	0.121714012	0.007575076	0.029454806	22477.8993	0.792633649
Main7	run0004	dmid	0.7	805.18	55.20967597	11.83118312	0.12622116	0.003344525	0.029454806	30534.7553	1.099267297
Main7	run0005	d-e	0.65	924.56	54.21710017	14.58708258	0.12381758	0.003326368	0.029454806	30595.55428	1.069916986
Main7	run0006	emid	0.6	1046.48	65.21542604	15.5846754	0.116208576	0.00330821	0.029454806	31032.76903	0.968640555
Main7	run0007	e-z	0.54	1163.32	69.61525518	14.9029806	0.120258	0.003152036	0.029454806	35514.49252	0.976930546
Main7	run0008	zmid	0.48	1290.32	65.63459538	15.11453436	0.113573743	0.002995862	0.029454806	34909.66652	0.927995074

Table 3: (cont.).

Run ID	UVPfile	Location	H (cm)	L (cm)	Kaolin %	AC%	U (m/s)	C (m3/m3)	Co (m3/m3)	Re #	Fr #
Main8	run0000	bmid	6	320.04	10.06910271	6.591318264	0.15318276	0.025018257	0.098305799	14458.92302	0.674152663
Main8	run0001	b-g	5	441.96	15.44785075	8.641728346	0.126655879	0.030080552	0.098305799	14280.30887	0.443781776
Main8	run0002	gmid	3.8	563.88	28.05476064	9.268146371	0.136469452	0.018875063	0.098305799	17427.37895	0.625254591
Main8	run0003	g-d	3	680.72	78.34946015	12.59377813	0.146064257	0.015108485	0.098305799	25289.01631	0.682351443
Main8	run0004	dmid	2.8	805.18	80.38946204	13.19395819	0.166230767	0.011341908	0.098305799	28799.19428	0.893360598
Main8	run0005	d-e	2.5	924.56	98.97974593	12.54125413	0.146610672	0.011195267	0.098305799	29356.5984	0.738396848
Main8	run0006	emid	2.2	1046.48	98.46859365	13.23264653	0.15501356	0.011048627	0.098305799	30249.48922	0.796834993
Main8	run0007	e-z	2.1	1163.32	96.26692109	17.12828717	0.133875311	0.01159785	0.098305799	30304.24935	0.621390941
Main8	run0008	zmid	2	1290.32	90.10346259	16.70334067	0.126346259	0.012147074	0.098305799	25574.76991	0.603727861
*Bound4	run0001	bmid	5.5	320.04	99	20.97392218	0.155547448	0.013212816	0.197032043	14113.15573	1.060471032
Bound4	run0002	b-g	4.75	441.96	99	23.23	0.133484145	0.013121113	0.197032043	16391.75053	0.782566864
Bound4	run0003	gmid	4.25	563.88	99	22.6084783	0.081290749	0.012592888	0.197032043	10793.23199	0.469592506
Bound4	run0004	g-d	4.1	680.72	99	28.2389761	0.10226281	0.012083887	0.197032043	17195.74892	0.537761877
Bound4	run0005	dmid	4	805.18	99	24.57191438	0.120239725	0.011574887	0.197032043	22443.07523	0.615309645
Bound4	run0006	d-e	3.8	924.56	99	27.94388561	0.139423501	0.011953622	0.197032043	24617.96164	0.72001454
Bound4	run0007	emid	3.8	1046.48	99	31.07465291	0.124616372	0.012332357	0.197032043	24279.69203	0.601593401
Bound4	run0008	e-z	3.5	1163.32	99	35.52290458	0.136910315	0.012308498	0.197032043	26683.79	0.661583476
Bound4	run0009	zmid	3.4	1290.32	99	38.98740252	0.127650327	0.012284639	0.197032043	22824.03125	0.64473874
Main9	run0001	bmid	1.6	320.04	32.42375783	13.09738052	0.104106851	0.013360086	0.049112941	11739.13194	0.632484907
Main9	run0002	b-g	1.2	441.96	56.31645364	11.36	0.106945865	0.016677295	0.049112941	12676.8813	0.552996281
Main9	run0003	gmid	1.3	563.88	60.5862661	14.40261679	0.110511451	0.010555024	0.049112941	16295.73431	0.670727442
Main9	run0004	g-d	1.3	680.72	63.78831312	17.44523357	0.10792061	0.009530788	0.049112941	18524.69978	0.642906374
Main9	run0005	dmid	1.1	805.18	84.00124547	17.08341668	0.121375214	0.008506551	0.049112941	20823.29877	0.77006148
Main9	run0006	d-e	1.15	924.56	89.7592533	18.29817018	0.133020142	0.007377276	0.049112941	22429.23114	0.919578214
Main9	run0007	emid	1.2	1046.48	89.05367373	23.12768723	0.146467	0.006248001	0.049112941	32154.98607	0.969410536
Main9	run0008	e-z	1.1	1163.32	98.54926822	17.69	0.125504575	0.005751733	0.049112941	23029.24962	0.949019693
Main9	run0009	zmid	1	1290.32	85.02137643	21.43643093	0.117558688	0.005255465	0.049112941	21230.22692	0.939287637
Bound5	run0001	bmid	1	320.04	98.7	15.59311862	0.119938598	0.013784355	0.030281936	11503.96449	0.775414988
Bound5	run0002	b-g	0.9	441.96	98.7	13.67136714	0.114566413	0.013501264	0.030281936	13309.27713	0.678901598
Bound5	run0003	gmid	1	563.88	0	13.67136714	0.139365327	0.010349572	0.030281936	19496.41683	0.878124952
Bound5	run0004	g-d	1	680.72	0	19.5419542	0.132511385	0.009218483	0.030281936	22272.60189	0.812630519
Bound5	run0005	dmid	1.1	805.18	0	23.89477896	0.135387752	0.008087395	0.030281936	25781.86053	0.838065977
Bound5	run0006	d-e	1.05	924.56	0	26.72309061	0.134726995	0.006597249	0.030281936	31423.55776	0.840574032
Bound5	run0007	emid	1	1046.48	0	29.55140226	0.139496049	0.005107104	0.030281936	28068.45869	1.071754503

Table 3: (cont.).

Run ID	UVPfile	Location	H (cm)	L (cm)	Kaolin %	AC%	U (m/s)	C (m3/m3)	Co (m3/m3)	Re #	Fr #
Bound5	run0008	e-z	0.95	1163.32	0	32.37971391	0.138341308	0.004442601	0.030281936	31163.30292	1.079657336
Bound5	run0009	zmid	0.9	1290.32	0	34.93	0.112211902	0.003778099	0.030281936	28605.60035	0.894593912
Main10	run0001	bmid	0.6	320.04	81.16144937	16.68166817	0.06107371	0.005241181	0.009968268	8806.762237	0.548917479
Main10	run0002	b-g	0.3	441.96	89.50218469	22.4155169	0.074042398	0.005800988	0.009968268	12238.69363	0.589470418
Main10	run0003	gmid	0.35	563.88	83.88844926	21.21212121	0.125570516	0.001844579	0.009968268	19715.21629	1.83383057
Main10	run0004	g-d	0.25	680.72	70.49965749	38.57543017	0.117095384	0.001503344	0.009968268	21926.10615	1.735344017
Main10	run0005	dmid	0.2	805.18	99.77354922	39.06771509	0.126219795	0.00116211	0.009968268	30973.19172	1.859183245
Main10	run0006	d-e	0.15	924.56	63.47259495	39.56	0.135244397	0.001078479	0.009968268	32136.50351	2.101615909
Main10	run0007	emid	0.15	1046.48	72.10834864	39.04219156	0.103968948	0.000994848	0.009968268	25404.17568	1.658948773
Main10	run0008	e-z	0.1	1163.32	77.43745371	41.28337201	0.099930869	0.000868614	0.009968268	27432.58233	1.610083059
Main10	run0009	zmid	0.1	1290.32	69.57338323	43.52455246	0.094908809	0.000742381	0.009968268	20761.2552	1.853082349
*Main11	run0001	bmid	1.85	320.04	0	1.86	0.088812499	0.002102904	0.030105573	14217.87652	1.205776557
Main11	run0002	b-g	1.6	441.96	0	3.219678032	0.091659941	0.00182742	0.030105573	17326.78186	1.229058959
Main11	run0003	gmid	1.25	563.88	0	4.66139842	0.060902233	0.00159889	0.030105573	9000.110795	0.984048558
Main11	run0004	g-d	0.7	680.72	0	5.051010202	0.070961267	0.001487535	0.030105573	11066.57119	1.157321922
Main11	run0005	dmid	0.8	805.18	0	5.838248525	0.04251408	0.00137618	0.030105573	10183.60674	0.581741907
Main11	run0006	d-e	0.9	924.56	0	5.860586059	0.045218174	0.001297979	0.030105573	11568.77107	0.616522296
Main11	run0007	emid	0.8	1046.48	0	7.289271073	0.051786695	0.001219778	0.030105573	13021.59888	0.734760751
Main11	run0008	e-z	1	1163.32	0	9.050905091	0.032914721	0.001342639	0.030105573	7398.097857	0.470740425
Main11	run0009	zmid	0.9	1290.32	0	9.216451516	0.03	0.001465499	0.030105573	5993.110346	0.435549041
Main12	run0001	bmid	2.4	320.04	23.06493599	14.82703459	0.137482433	0.011658673	0.100029286	17206.9713	0.85797742
Main12	run0002	b-g	2.2	441.96	55.82047547	13.85138514	0.158522338	0.012965711	0.100029286	20433.22796	0.916073882
Main12	run0003	gmid	2.1	563.88	47.25165127	25.92259226	0.160754161	0.013360559	0.100029286	20604.05952	0.91172415
Main12	run0004	g-d	2.3	680.72	85.70006911	17.63470959	0.144635788	0.012875397	0.100029286	22131.1836	0.767442682
Main12	run0005	dmid	2.4	805.18	97.97254412	15.95319064	0.126449674	0.012390235	0.100029286	21682.57801	0.648294554
Main12	run0006	d-e	2.5	924.56	69.84138669	25.96480704	0.115103513	0.012634359	0.100029286	25816.85089	0.510101672
Main12	run0007	emid	2.2	1046.48	98.5294658	19.19191919	0.122503702	0.012878483	0.100029286	30805.1324	0.506973635
Main12	run0008	e-z	2.1	1163.32	73.40449903	26.72534507	0.115078735	0.012741045	0.100029286	29991.38517	0.470780648
Main12	run0009	zmid	2	1290.32	90.2748592	23.79237924	0.09609614	0.012603606	0.100029286	23038.95798	0.412501691
RF1	Profile02	bmid	2	320.04	0	17	0.104110948	0.003639837	0.029935603	16797.57388	1.066309153
RF1	Profile03	b-g	1	441.96	0	18.76718015	0.100686739	0.00325004	0.029935603	16872.42059	1.0720118
RF1	Profile04	gmid	0.7	563.88	0	24.03625363	0.144435837	0.003348503	0.029935603	25464.01715	1.471154873
RF1	Profile05	g-d	0.5	680.72	0	38.44455554	0.117546209	0.003735866	0.029935603	24985.5017	1.031165601
RF1	Profile06	dmid	0.35	805.18	0	51.5935187	0.129408224	0.004123228	0.029935603	28197.70115	1.065981045

Table 3: (cont.).

Run ID	UVPfile	Location	H (cm)	L (cm)	Kaolin %	AC%	U (m/s)	C (m3/m3)	Co (m3/m3)	Re #	Fr #
RF1	Profile07	d-e	0.28	924.56	0	53.19064719	0.134868525	0.00381801	0.029935603	33099.55731	1.088890225
RF1	Profile08	emid	0.25	1046.48	0	54.42993828	0.113822721	0.003512792	0.029935603	27149.19894	0.972692364
RF1	Profile09	e-z	0.23	1163.32	0	59.40811838	0.122568531	0.003544816	0.029935603	30219.26426	1.025479326
RF1	Profile10	zmid	0.22	1290.32	0	58.61	0.146136605	0.00357684	0.029935603	51461.94653	1.018363983